551548

Cloud Microphysics Budget in the Tropical Deep Convective Regime

Xiaofan Li[1], C.-H. Sui[2], K.-M. Lau

NASA/Goddard Space Flight Center, Greenbelt, Maryland

Submitted to J. Meteor. Soc. Japan

March, 2001

[1]Current affiliation: NOAA/NESDIS/ORA/ARAD, Camps Spring, MD

[2]Corresponding author address: Dr. C.-H. Sui, NASA/GSFC, Code 913, Greenbelt, MD 20771 < *email* > sui@climate.gsfc.nasa.gov

Abstract

Cloud microphysics budgets in the tropical deep convective regime are analyzed based on a 2-D cloud resolving simulation. The model is forced by the large-scale vertical velocity and zonal wind and large-scale horizontal advections derived from TOGA COARE for a 20-day period. The role of cloud microphysics is first examined by analyzing mass-weighted mean heat budget and column-integrated moisture budget. Hourly budgets show that local changes of mass-weighted mean temperature and column-integrated moisture are mainly determined by the residuals between vertical thermal advection and latent heat of condensation and between vertical moisture advection and condensation respectively. Thus, atmospheric thermodynamics depends on how cloud microphysical processes are parameterized.

Cloud microphysics budgets are then analyzed for raining conditions. For cloud-vapor exchange between cloud system and its embedded environment, rainfall and evaporation of raindrop are compensated by the condensation and deposition of supersaturated vapor. Inside the cloud system, the condensation of supersaturated vapor balances conversion from cloud water to raindrop, snow, and graupel through collection and accretion processes. The deposition of supersaturated vapor balances conversion from cloud ice to snow through conversion and riming processes. The conversion and riming of cloud ice and the accretion of cloud water balance conversion from snow to graupel through accretion process. Finally, the collection of cloud water and the melting of graupel increase raindrop to compensate the loss of raindrop due to rainfall and the evaporation of raindrop.

1. Introduction

Cumulus parameterization has been one of major research issues for more than three decades in meteorological community since the atmospheric general circulation model (GCM) became a major research and operational tool. The main idea in the cumulus parameterization is to use the large-scale variables to estimate the amount of the precipitation and the net heating and moistening effects due to sub-scale disturbances (convection) that cannot be simulated in the GCM. Based on the observation that the tropical deep convection always occurs over the region of large-scale moisture convergence, Kuo (1965, 1974) used the temperature difference between the cumulus cloud and the surrounding environment, and the large-scale moisture convergence to calculate the net convergence of moisture into the vertical column of the air of unit cross section produced by the large-scale circulation, and by evaporation from the earth surface. The large part of the net moisture convergence is assumed to produce precipitation. Based on the assumption that the rate of production of available potential energy by the large-scale processes is nearly balanced by the rate of consumption of the available potential energy by the convection, Arakawa and Schubert (1974) used the vertical distributions of the total vertical mass flux by the cumulus cloud ensemble, the total detrainment of mass from the ensemble, and the thermodynamical properties of detraining air to parameterize the cumulus convection. Such physically and observationally based cumulus convection parameterizations have been included in the numerical models which lead to success of simulations of atmospheric circulations. Different from the cumulus parameterization, cloud microphysics parameterization uses the cloud thermodynamic variables to directly predict the cloud variations based on the empirical relationships derived from laboratory experiments and in-situ observations. The cloud resolving models that include cloud microphysics parameterization schemes have demonstrated to simulate reasonable atmospheric thermodynamics in the tropics during the GARP (Global Atmospheric Research Program) Atlantic Tropical Experiment (GATE: e.g., Xu and Randall 1996; Grabowski et al. 1996) and Tropical Ocean Global Atmosphere Coupled Ocean-Atmosphere Response Experiment (TOGA COARE: e.g., Wu et al. 1998; Li et al. 1999). Willoughby et al. (1984), Lord et al. (1984), and Liu et al. (1997) showed that inclusion of ice microphysics in their numerical models led to more realistic simula-

tions of cloud structures of model hurricanes. To understand how the cloud microphysics parameterization improve simulations, it is necessary to know the cloud microphysics budgets for cloud water, raindrop, cloud ice, snow, and graupel, and understand the dominant conversion processes and their growth and decay mechanisms.

In this study, the 2-D cloud resolving model is used to investigate the dominant cloud microphysical processes associated with tropical deep convection and their roles in atmospheric thermodynamics. In the next section, the cloud resolving model will be briefly described, and heat and moisture equations used in budget analyses will be derived. In section three, we will show that vertical potential temperature advection and latent heat of condensation, and vertical moisture advection and condensation are the largest terms, respectively, in the mass-weighted mean heat budget and in the column-integrated moisture budget. Further, the residuals between the two terms, respectively, accounts for hourly thermal and moisture variations, implying the fundamental importance of cloud microphysical processes in determining atmospheric thermodynamics. Thus, the cloud microphysics budgets are calculated to analyze the dominant cloud microphysical processes in the tropical deep convective regimes in section four. Scale analysis is conducted to explain dominant cloud microphysical processes. Summary is given in section six.

2. Formulations for model, heat, and moisture budgets

The cloud resolving model was originally developed by Soong and Ogura (1980), Soong and Tao (1980), and Tao and Simpson (1993). The 2-D version of the model used by Sui et al. (1998) and modified by Li et al. (1999) is used in this study. The governing equations with an anelastic approximation can be expressed as follows:

$$\frac{\partial u'}{\partial x} + \frac{1}{\overline{\rho}} \frac{\partial}{\partial z} \overline{\rho} w' = 0, \tag{1}$$

$$\frac{\partial u'}{\partial t} = -\frac{\partial}{\partial x}(u'\overline{u}^o + \overline{u}^o u' + u'u') - \frac{1}{\overline{\rho}} \frac{\partial}{\partial z} \overline{\rho}(w'\overline{u}^o + \overline{w}^o u' + w'u' - \overline{w'u'})$$

$$-c_p \frac{\partial}{\partial x}(\overline{\theta}\pi') + D_u - \overline{D}_u, \tag{2}$$

$$\frac{\partial w'}{\partial t} = -\frac{\partial}{\partial x}(u'\overline{w}^o + \overline{u}^o w' + u'w') - \frac{1}{\overline{\rho}}\frac{\partial}{\partial z}\overline{\rho}(w'\overline{w}^o + \overline{w}^o w' + w'w' - \overline{w'w'})$$

$$-c_p\frac{\partial}{\partial z}(\overline{\theta}\pi') + g(\frac{\theta'}{\theta_b} + 0.61q_v' - q_l') + D_w - \overline{D}_w, \tag{3}$$

$$\frac{\partial \theta}{\partial t} = -\frac{\partial(u'\theta')}{\partial x} - \overline{u}^o\frac{\partial \theta'}{\partial x} - \frac{1}{\overline{\rho}}\frac{\partial}{\partial z}\overline{\rho}w'\theta' - \overline{w}^o\frac{\partial \theta'}{\partial z} - w'\frac{\partial \overline{\theta}}{\partial z}$$

$$+\frac{1}{\pi c_p}Q_{cn} + \frac{1}{\pi c_p}Q_R - \overline{u}^o\frac{\partial \overline{\theta}^o}{\partial x} - \overline{w}^o\frac{\partial \overline{\theta}}{\partial z} + D_\theta, \tag{4}$$

$$\frac{\partial q_v}{\partial t} = -\frac{\partial(u'q_v')}{\partial x} - \overline{u}^o\frac{\partial q_v'}{\partial x} - \frac{1}{\overline{\rho}}\frac{\partial}{\partial z}\overline{\rho}w'q_v' - \overline{w}^o\frac{\partial q_v'}{\partial z} - w'\frac{\partial \overline{q}_v}{\partial z}$$

$$-(c - e + d - s) - \overline{u}^o\frac{\partial \overline{q_v}^o}{\partial x} - \overline{w}^o\frac{\partial \overline{q}_v}{\partial z} + D_{q_v}, \tag{5}$$

$$\frac{\partial C}{\partial t} = -\frac{\partial(uC)}{\partial x} - \frac{1}{\overline{\rho}}\frac{\partial}{\partial z}[\overline{\rho}(w - w_{TV})C] + S_C + D_C. \tag{6}$$

Here u, and w are zonal, and vertical air wind components; θ and q_v are air potential temperature and specific humidity respectively; $C = (q_c, q_r, q_i, q_s, q_g)$, q_c, q_r, q_i, q_s, and q_g are the mixing ratios of cloud water (small cloud droplets), raindrop, cloud ice (small ice crystals), snow (density 0.1 g cm^{-3}), and graupel (density 0.4 g cm^{-3}), respectively; $\overline{\rho}$ is a mean air density which is a function of height only; w_{TV} is a terminal velocity which is zero for cloud water and ice; π=$(p/p_o)^\kappa$, $\kappa = \frac{R}{c_p}$, R is the gas constant, c_p is the specific heat of dry air at constant pressure p, and p_o=1000 mb; c, e, d, and s denote condensation, evaporation, deposition, and sublimation, respectively; $Q_{cn} = L_v(c-e)+L_s(d-s)+L_f(f-m)$ denotes the net latent heat release through phase changes among different cloud species, where f and m are fusion and melting, respectively; L_v, L_s, and L_f are heat coefficients due to phase changes; Q_R is the radiative heating rate due to convergence of net flux of solar and infrared radiative fluxes; S_C is source and sink of cloud content determined by cloud microphyical processes (see Appendix); Ds are dissipation terms; overbar ($^-$)

denotes a zonal-mean; subscript $_b$ denotes an initial value, which does not vary with time; superscript ^{o} denotes imposed observed variables in the model.

To examine domain-mean heat and moisture budgets, the equations for $\overline{T}$ $(= \pi\overline{\theta})$ and $\overline{q_v}$ are derived from (6),

$$\frac{\partial \overline{T}}{\partial t} = \frac{1}{c_p}\overline{Q}_{cn} + \frac{1}{c_p}\overline{Q}_R - \frac{\pi}{\overline{\rho}}\frac{\partial}{\partial z}\overline{\rho w'\theta'} - \pi\overline{w}^o\frac{\partial \overline{\theta}}{\partial z} - \overline{u}^o\frac{\partial \overline{T}^o}{\partial x}, \tag{7a}$$

$$\frac{\partial \overline{q}_v}{\partial t} = -(\overline{c} - \overline{e} + \overline{d} - \overline{s}) - \frac{1}{\overline{\rho}}\frac{\partial}{\partial z}\overline{\rho w'q_v'} - \overline{w}^o\frac{\partial \overline{q}_v}{\partial z} - \overline{u}^o\frac{\partial \overline{q}_v^o}{\partial x}, \tag{7b}$$

For mass-weighted mean heat budget, multiplying (7a) by $\overline{\rho}$, and integrating the resulting equation vertically, and dividing it by the mass of the air column yield

$$\frac{\partial < \overline{T} >}{\partial t} = \frac{1}{c_p} < \overline{Q}_{cn} > + \frac{1}{c_p} < \overline{Q}_R > + \overline{H}_s - < \pi\overline{w}^o\frac{\partial \overline{\theta}}{\partial z} > - < \overline{u}^o\frac{\partial \overline{T}^o}{\partial x} >, \tag{8a}$$

and for column-integrated water vapor budget, multiplying (7b) by $\overline{\rho}$, and integrating the resulting equation vertically yield

$$\frac{\partial [\overline{q}_v]}{\partial t} = -\overline{P} + \overline{E} - [\overline{w}^o\frac{\partial \overline{q}_v}{\partial z}] - [\overline{u}^o\frac{\partial \overline{q}_v^o}{\partial x}]. \tag{8b}$$

Here $< () >= [()]/[1]$, and $[()] = \int_0^{z_T} \overline{\rho}()dz$, where z_T is the height of top model level. $\overline{H}_s$, - $\overline{P}$, and $\overline{E}$ are surface sensible heat flux, precipitation, and surface evaporation, respectively.

3. Mean-weighted mean heat budget and column-integrated moisture budget

The experiment analyzed in this study is conducted with the model forced by zonally uniform vertical velocity, zonal wind, and horizontal advections, which are derived by Professor Minghua Zhang who used the 6-hourly TOGA COARE observations within the Intensive Flux Array (IFA) region. The calculations are based on the constrained variational method on column-integrated budgets of mass, heat, moisture, and momentum proposed by Zhang and Lin (1997). Hourly sea surface temperature at the Improved

Meteorological (IMET) surface mooring buoy ($1.75^oS, 156^oE$) (Weller and Anderson 1996) is also imposed in the model. The model is integrated from 0400 19 December 1992 to 0400 9 January 1993 (local time). The horizontal domain is 768 km. A grid mesh of 1.5 km and a 12 second step are used in model integrations. More discussion of the model is reported in Li et al. (1999). Hourly simulation data are analyzed in the following discussions.

Figure 1 shows the time evolution of vertical distribution of the large-scale atmospheric vertical velocity and zonal wind during 19 December 1992-9 January 1993 that are imposed in the model. Within 19-25 December 1992, upward motion was dominant, indicating strong convection. From 26 December 1992-3 January 1993, downward motion became dominant, along with occasional upward motion, suggesting the dry phase. In the last few days, moderate upward motion occurred. The diurnal and two-day signals are also detected in Fig.1a as indicated by Sui et al. (1997) and Takayabu et al. (1996) respectively. The large-scale westerly winds increase significantly in the lower- and mid- troposphere and reach their maximum of $20ms^{-1}$ at 600 mb around 3 January 1993 (Fig. 1b). As mentioned previously, the model is also forced by the observed horizontal temperature and moisture advections (not shown), which have much smaller amplitudes than the vertical advections respectively.

The comparison between simulation and observation is carried out by analyzing the linear correlation coefficients and the RMS of temperature and specific humidity, which are shown in Fig. 2. The correlation can be as high as 0.7 for temperature only in the upper troposphere and near the surface, and it becomes lower in the mid- and lower-troposphere with the minimum of 0.1 around 730 mb. The correlation of specific humidity is about 0.7 between 300 and 700 mb, but it reaches its minimum of 0.1 around 870 mb. The RMS of temperature increases from 0.7 ^oC near the surface to 2.5 ^oC around 200 mb, whereas the RMS of specific humidity is 0.15-0.75 gkg^{-1}. Some explanations of differences between simulation and observation can be referred to Li et al. (1999).

Fig. 3 shows the each term of mass-weighted mean heat budget and column-integrated moisture budget versus local changes of mean-weighted mean temperature and column-integrated moisture (precipitable water) respectively. In the heat budget, the local changes

of mass-weighted mean temperature are mainly caused by the sum of latent heat of condensation and vertical potential temperature advection, because of small horizontal thermal advection and surface sensible heat flux, and nearly constant radiative cooling (Fig. 3a). In the moisture budget, the local changes of precipitable water are mainly due to sum of precipitation and vertical moisture advection, since the small horizontal moisture advection, and nearly constant surface evaporation (Fig. 3b).

Fig. 4 shows that the latent heat of condensation and vertical potential temperature advection in mass-weighted mean heat budget and the precipitation and vertical moisture advection in column-integrated moisture budget have same orders of magnitudes but the opposite signs, indicating these terms cancel in large parts. To examine the dependence of the residuals between these largest terms on intensity of convection, we plotted the sum of mass-weighted mean latent heat of condensation and vertical potential temperature advection, and sum of condensation and column-integrated vertical moisture advection versus rain rates in Fig. 5. The thermal sum increases from small negative values to relatively large positive values as the rain rate increases (Fig. 5a), whereas the moisture sum decreases from small positive values to relatively negative values as the rain rate increases (Fig. 5b). Atmosphere tends to be warmed and dryed when surface rain rate is larger than 30 $mmday^{-1}$.

Figs. 3-5 indicate that the cloud microphysics parameterization is very crucial to determine the atmospheric thermodynamics. The dominant effect of sum of latent heat of condensation and vertical potential temperature advection on temperature variation is also evident in the mid-troposphere (309, 487, and 694 mb) as shown in Fig. 6. In the upper-troposphere (194 mb), the increase of temperature is mainly due to vertical heat flux convergence, whereas the decrease of temperature results from radiative cooling (Fig. 6a). In the lower-troposphere (907 mb), vertical heat flux convergence, the latent heat of condensation, and vertical potential temperature advection are responsible for temperature variations (Fig. 6e).

The dominant effect of sum of condensation and vertical moisture advection on moisture variations is only seen at 487 mb (Fig. 7c). In the upper-troposphere (194 mb and 309

mb), the condensation and vertical moisture advection and vertical moisture flux convergence cancel each other (Figs. 7a and 7b). In the lower-troposphere (694 mb and 907 mb), vertical moisture flux convergence is an important factor for the local moisture changes (Figs. 7d and 7e). Although the sum of condensation and vertical moisture advection is the dominant factor in column-integrated moisture budget, the vertical moisture flux convergence is the important process at the individual vertical levels.

4. Dominant cloud microphysical processes

Before discussion of dominant cloud microphysical processes, column-integrated cloud contents versus surface rain rate and vertical structures of mean cloud contents are examined (Fig. 8). Cloud water, raindrop, graupel, and total cloud contents increase with increasing surface rain rate, whereas cloud ice and snow are much less sensitive to surface rain rate. Maximum of total cloud contents is between 500 and 600 mb, which is largely contributed by graupel, raindrop, and cloud water. Maxima of cloud ice and snow appear around 250 mb and 350 mb levels respectively.

There are two aspects of cloud microphysical processes: cloud-vapor exchange between the cloud system and its embedded environment, and conversions among cloud contents inside the cloud system. In this study, notations for cloud microphysics are consistent with the previous studies. The rate of conversion for cloud microphysics is always denoted by a positive value, and the sign before the conversion term represents the direction conversion goes to. For cloud-vapor exchange between cloud system and the environment, there are seven cloud microphysical processes (see A1a). Only three of them are important (Fig. 9a). Two sinks for vapors are conversion from vapor to cloud water by the condensation of supersaturated vapor ($-P_{CND}$) and conversion from vapor to cloud ice by the deposition of supersaturated vapor ($-P_{DEP}$). One source for vapor are conversion from raindrop to vapor by evaporation of raindrop (P_{REVP}). Vertical profiles of mean cloud microphysical processes (Fig. 9b) display that the maxima of P_{CND} and P_{DEP} are at 600 mb and 350 mb levels respectively. The P_{REVP} increases from 500 mb to 700 mb, and keep the constant below 700 mb level.

Inside the cloud system, there are nine cloud microphysical processes for cloud water (see A1b). Three of them are dominant (Fig. 10). Two sinks for cloud water are growth of raindrop by the collection of cloud water (-P_{RACW}) and growth of graupel by the accretion of cloud water (-P_{GACW}). One source for cloud water is growth of cloud water by the condensation of supersaturated vapor (P_{CND}). Although it is relatively small, growth of snow by the accretion of cloud water (-P_{SACW}) is also included to close the budget. Since the sum of these cloud microphysical processes are much smaller than the dominant processes, the condensation of supersaturated vapor maintains conversion from cloud water to raindrop, snow, and graupel by the collection and accretion of cloud water respectively. The large positive values of P_{CND} are between 550 mb and 850 mb, whereas the large negative values of P_{RACW} and P_{GACW} are around 600-800 mb and 550 mb level respectively. Four terms cancel each other in large part (Fig. 15a). The sum of these terms show maximum positive values at 900 mb level and maximum negative value at 550 mb, and their magnitudes are about the same so that column-integrated sum is near zero.

For raindrop, there are twelve cloud microphysical processes (see A1c). Three of them are important (Fig. 11). Two sources for raindrop are the collection of cloud water (P_{RACW}) and the melting of graupel (P_{GMLT}). One sink for raindrop is growth of vapor by evaporation of raindrop (-P_{REVP}) The sum of the rates of these processes is linearly proportional to surface rain rate. Thus, rainfall and evaporation of raindrop are compensated by melting of graupel and collection of cloud water. The maximum of cloud microphysical processes related to raindrop is at about 570 mb level, which is mainly contributed by P_{GMLT}, as well as P_{RACW} (Fig. 15b). P_{RACW} and -P_{REVP} have the similar vertical structures but have the opposite signs. Thus, P_{RACW} and -P_{REVP} cancel each other in large parts.

For cloud ice, there are nine cloud microphysical processes (see A1d). Three of them are important (Fig. 12). Two sinks for cloud ice are growth of snow by the conversion of cloud ice (-P_{SAUT}) and by the riming of cloud ice (-P_{SFI}). One source for cloud ice is the deposition of supersaturated vapor (P_{DEP}). Since the sum is about zero, the deposition of supersaturated vapor maintains conversion from cloud ice to snow through

conversion and riming of cloud ice. Maximum positive value of P_{DEP} occurs at 350 mb level, whereas maximum negative values of P_{SAUT} and P_{SFI} appear at 400 mb and 250 mb levels respectively (Fig. 15c). Maximum positive and negative values of the sum are at 200 mb and 300 mb levels respectively, and they have similar magnitudes that lead to a near-zero column integration.

For snow, there are fifteen cloud microphysical processes (see A1e). Four of them are important (Fig. 13). Three sources for snow are the conversion of cloud ice (P_{SAUT}), the riming of cloud ice (P_{SFI}), and the accretion of cloud water (P_{SACW}, note $\delta_4 = 1$ here). One sink for snow is growth of graupel by the accretion of snow ($-P_{GACS}$). Since the sum is almost zero, the growth of graupel by the accretion of snow is nearly balanced by the conversion from cloud ice to snow through the conversion and riming processes, and conversion from cloud water to snow through the accretion process. Maximum positive values of P_{SAUT}, P_{SFI}, and P_{SACW} are at 400 mb, 250 mb, and 500 mb levels respectively. Maximum negative value of $-P_{GACS}$ is at 370 mb level with the second maximum negative value at 530 mb level (Fig. 15d). The sum has a maximum positive value at 250 mb level, which is mainly contributed by P_{SFI}, and a maximum negative value at 570 mb, which is mainly contributed by $-P_{GACS}$. Column-integrated sum is about zero.

For graupel, there are fourteen cloud microphysical processes (see A1f). Three of them are important (Fig. 14). Two sources for graupel are the accretion of cloud water (P_{GACW}) and the accretion of snow (P_{GACS}). One sink for graupel is growth of raindrop by melting of graupel ($-P_{GMLT}$). Since the sum is much smaller than the dominant processes, melting of graupel is compensated by the accretion of cloud water and snow. Vertical structures of mean cloud microphysical processes (Fig. 15e) show that the sum has a maximum negative value at 570 mb level, which is contributed by $-P_{GMLT}$, and maximum positive value at 500 mb level, which is contributed by P_{GACW} and P_{GACS}. Thus, the column-integrated sum becomes very small.

Figure 16 summarizes mean column-integrated cloud microphysical budget. For exchange between cloud system and the atmospheric environment, rain rate (10.6 mm day^{-1}) and evaporation of raindrop (6.4 mm day^{-1}) are nearly compensated by the condensation

(14.0 mm day^{-1}) and deposition (2.5 mm day^{-1}) of supersaturated vapor. Inside the cloud system, the condensation of supersaturated vapor (14.0 mm day^{-1}) supports conversion from cloud water to raindrop (9.4 mm day^{-1}), snow (0.9 mm day^{-1}), and graupel (3.3 mm day^{-1}) through the collection and accretion processes. The deposition of supersaturated vapor (2.5 mm day^{-1}) supports the conversion from cloud ice to snow through the conversion (1.6 mm day^{-1}) and riming (0.7 mm day^{-1}) processes. The conversion and riming of cloud ice and the accretion of cloud water maintain the conversion from snow to graupel by the accretion process (3.0 mm day^{-1}). Finally, the collection of cloud water (9.4 mm day^{-1}) and the melting of graupel (6.5 mm day^{-1}) increase raindrop to balance the loss of raindrop due to precipitation (10.6 mm day^{-1}) and evaporation of raindrop (6.4 mm day^{-1}).

5. Scale analysis

The source for development of clouds stems from the difference between atmospheric specific humidity and saturation specific humidity for water and ice. The schemes of Tao et al. (1989) for calculations of P_{CND} (A7) and P_{DEP} (A17) indicate that the sum of P_{CND} and P_{DEP} is linearly proportional to the difference and is modified by temperature and mixing ratios of cloud water and ice. P_{CND} and P_{DEP} are partitioned by the linear function of temperature. Reference temperatures are T_{00} for P_{CND} and T_0 for P_{DEP} so that magnitude of P_{CND} is much larger than that of P_{DEP}. The major sink of clouds is P_{REVP} (A5). For the evaporation and deposition processes (A3, A4, A5, A24, A30), the second terms are larger than the first terms. Thus, the ratios of $[P_{REVP}]$ to $[P_{MLTG}]$, $[P_{REVP}]$ to $[P_{MLTS}]$, $[P_{REVP}]$ to $[P_{SDEP}]$, and $[P_{REVP}]$ to $[P_{GDEP}]$ can be estimated by

$$\frac{[P_{REVP}]}{[P_{MLTG}]} \sim (\frac{a'}{\overline{a}})^{\frac{1}{2}} \frac{[(S-1)(\frac{q_r}{\rho})^{\frac{3}{4}}]}{[(S-1)(\frac{q_g}{\rho})^{\frac{b+5}{2}}]} \sim (\frac{a'}{\overline{a}})^{\frac{1}{2}}, \tag{9a}$$

$$\frac{[P_{REVP}]}{[P_{MLTS}]} \sim (\frac{a'}{a''})^{\frac{1}{2}} \frac{[(S-1)(\frac{q_r}{\rho})^{\frac{3}{4}}]}{[(S-1)(\frac{q_s}{\rho})^{\frac{b+5}{2}}]} \sim (\frac{a'}{a''})^{\frac{1}{2}}, \tag{9b}$$

$$\frac{[P_{REVP}]}{[P_{SDEP}]} \sim (\frac{a'}{a''})^{\frac{1}{2}} \frac{[(S-1)(\frac{q_r}{\rho})^{\frac{3}{4}}]}{[(S_i-1)(\frac{q_s}{\rho})^{\frac{b+5}{2}}]} \sim (\frac{a'}{a''})^{\frac{1}{2}}, \tag{9c}$$

$$\frac{[P_{REVP}]}{[P_{GDEP}]} \sim (\frac{a'}{\overline{a}})^{\frac{1}{2}} \frac{[(S-1)(\frac{q_r}{\rho})^{\frac{3}{4}}]}{[(S_i-1)(\frac{q_g}{\rho})^{\frac{\overline{b}+5}{2}}]}) \sim (\frac{a'}{\overline{a}})^{\frac{1}{2}}. \tag{9d}$$

In estimation of (9), the fact that the covariance between $S-1$ and q_r is larger than the covariances between $S-1$ (S_i-1) and q_s and between $S-1$ (S_i-1) and q_g is considered. The raindrop has larger falling velocity than snow and graupel. Thus, $(\frac{a'}{\overline{a}})^{\frac{1}{2}} \sim 12.5$, $(\frac{a'}{a''})^{\frac{1}{2}} \sim 51.3$. Therefore, $[P_{REVP}]$ is more than one order of magnitude larger than $[P_{SDEP}]$, $[P_{MLTS}]$, $[P_{GDEP}]$, and $[P_{MLTG}]$.

For the melting processes, the second terms of P_{GMLT} (A8) and P_{SMLT} (A9) are much larger than the first terms. The ratio of $[P_{GMLT}]$ to $[P_{SMLT}]$ can be expressed by

$$\frac{[P_{GMLT}]}{[P_{SMLT}]} \sim (\frac{\overline{a}}{a'})^{\frac{1}{2}} \frac{[(T-T_0)(\frac{q_g}{\rho})^{\frac{\overline{b}+5}{2}}]}{[(T-T_0)(\frac{q_s}{\rho})^{\frac{b+5}{2}}]}. \tag{10}$$

The graupel has larger falling speed and mixing ratio than does the snow. Thus, $(\frac{\overline{a}}{a'})^{\frac{1}{2}} = 4.1$. The magnitude of q_g is twice as large as that of q_s. Therefore, $[P_{GMLT}]$ is about one order of magnitude larger than $[P_{SMLT}]$.

For the accretion and collection processes, the second terms of P_{RACI} (A10), P_{RACW} (A11), and P_{IACR} (A15) are much larger than the other terms. The ratio of $[P_{RACW}]$ to $[P_{RACI}]$ becomes

$$\frac{[P_{RACW}]}{[P_{RACI}]} \sim \frac{[\rho^{-\frac{1}{2}} q_c q_r]}{[\rho^{-\frac{1}{2}} q_i q_r]}, \tag{11}$$

q_c and q_r are large in the mid and lower troposphere, whereas q_i are large in the upper troposphere. Thus, the covariance between q_c and q_r is much larger than the covariance between q_i and q_r. $[P_{RACW}]$ is at least one order of magnitude larger than $[P_{RACI}]$. Similar analysis shows $[P_{RACW}]$ is one order of magnitude larger than $[P_{IACR}]$. For the accretion processes, P_{GACS} (A27) is proportional to the covariance between q_s and q_g, whereas P_{RACS} (A11), P_{SACR} (A23), and P_{GACR} (A26) are proportional to the covariances between q_r and q_s and between q_r and q_g. Since the covariance between q_s and q_g is much larger than the covariances between q_r and q_s and between q_r and q_g, $[P_{GACS}]$ is much larger than other three processes.

For the accretion, collection, and riming processes, the collection efficiency coefficients of P_{SACW} (A20), P_{GACW} (A28), and P_{WACS} (A29) are one order of magnitude larger than those of P_{SACI} (A19) and P_{GACI} (A25). The falling speed coefficient of the graupel ($\overline{a}$) is more than one order of magnitude larger than that of the snow (a''). Thus, $[P_{GACW}]$ is the largest process compared to other four processes.

Since the second term is larger than the first term in P_{SAUT} (A18), and Δt_1 has the similar magnitude as Δt in P_{SFI} (A22), $[P_{SAUT}]$ and $[P_{SFI}]$ have same orders of magnitudes. P_{SAUT} and P_{SFI} occur when $T < T_0$, whereas P^{IMLT} (A16) occurs when $T > T_0$. $[\frac{\Delta t}{m_{ir}}(a_1 m_{ir}^{a_2} + \pi \rho q_c r^2 U_{ir})]$ of P_{SFW} (A21) is very small (not shown). Therefore, magnitudes of $[P_{SAUT}]$ and $[P_{SFI}]$ are much larger than those of $[P_{IMLT}]$ and $[P_{SFW}]$. Since cloud ice hardly exceeds the threshold, P_{RAUT} (A13) is small. Mixing ratio of cloud water is small when $T < T_{00}$. Thus, $[P_{IHOM}]$ is negligible. Calculation indicates that $|\frac{q_i n_0}{\rho m_{ir}} e^{0.5|T-T_0|}| < 0.01$. $[P_{IDW}]$ is at least one order of magnitude smaller than $[P_{SFW}]$.

6. Summary

Dominant cloud microphysical processes and their roles in atmospheric thermodynamics are investigated by using a 2-D cloud resolving model. The model is integrated for 20 days under the forcing of large-scale vertical velocity and zonal wind, as well as the large-scale horizontal advections derived from TOGA COARE data. Analyses of the hourly mass-weighted mean heat budget and the hourly column-integrated moisture budget show that the local changes of temperature and moisture are mainly caused by residuals between vertical thermal advection and latent heat of condensation and between vertical moisture advection and condensation respectively. This indicates that the cloud microphysical processes play important roles in determining atmospheric thermodynamics.

Two important aspects of cloud microphysical processes are cloud-environment interaction and interactions among cloud contents. The cloud-environment interaction is represented by cloud-vapor exchange between cloud system and its embedded environment. This exchange eventually affects the development of convection and atmospheric thermodynamics. The mean cloud microphysics budget shows that precipitation and evaporation

of raindrop are largely compensated by the condensation and deposition of supersaturated vapor. The interactions among cloud contents are represented by the conversion among cloud contents, which are associated with collection, conversion, accretion, and riming processes. The condensation of supersaturated vapor converts vapor into cloud water. The collection and accretion of cloud water further enhance raindrop, snow, and graupel respectively. The deposition of supersaturated vapor converts vapor into cloud ice. The conversion and riming of cloud ice and the accretion of cloud water generate snow, and the accretion of snow produces graupel. Finally, the collection of cloud water and melting of graupel balance the loss of raindrop due to rainfall and its evaporation.

Acknowledgments. Authors thank Prof. M. Zhang at the State University of New York at Stony Brook for allowing us to use his TOGA COARE forcing data. This research is supported under the TRMM projects of NASA's Mission to Planet Earth Office.

Appendix

Microphysical processes parameterized in cloud resolving model

Microphysics parameterizations in the cloud resolving model used in this study are based on the schemes proposed by Rutledge and Hobbs (1983, 1984; referred to as RH83 and RH84 thereafter), Lin et al., (1983; LFO), Tao et al. (1989; TSM), and Krueger et al. (1995; KFLC) respectively. Corresponding equations are as follows.

$$S_{q_v} = -P_{CND} - P_{DEP} - (1-\delta_1)P_{SDEP}(T<T_0) - (1-\delta_1)P_{GDEP}(T<T_0)$$
$$+P_{REVP} + P_{MLTG}(T>T_0) + P_{MLTS}(T>T_0), \qquad (A1a)$$

$$S_{q_c} = -P_{SACW} - P_{RAUT} - P_{RACW} - P_{SFW}(T<T_0) - P_{GACW} + P_{CND}$$
$$-P_{IHOM}(T<T_{00}) + P_{IMLT}(T>T_0) - P_{IDW}(T_{00}<T<T_0), \qquad (A1b)$$

$$S_{q_r} = P_{SACW}(T>T_0) + P_{RAUT} + P_{RACW} + P_{GACW}(T>T_0) - P_{REVP}$$
$$+P_{RACS}(T>T_0) - P_{IACR}(T<T_0) - P_{GACR}(T<T_0) - P_{SACR}(T<T_0)$$
$$-P_{GFR}(T<T_0) + P_{SMLT}(T>T_0) + P_{GMLT}(T>T_0), \qquad (A1c)$$

$$S_{q_i} = -P_{SAUT}(T<T_0) - P_{SACI}(T<T_0) - P_{RACI}(T<T_0) - P_{SFI}(T<T_0)$$
$$-P_{GACI}(T<T_0) + P_{IHOM}(T<T_{00}) - P_{IMLT}(T>T_0) + P_{DEP}$$
$$+P_{IDW}(T_{00}<T<T_0), \qquad (A1d)$$

$$S_{q_s} = P_{SAUT}(T<T_0) + P_{SACI}(T<T_0) + \delta_4 P_{SACW}(T<T_0) + P_{SFW}(T<T_0)$$

$$+P_{SFI}(T<T_0)+\delta_3 P_{RACI}(T<T_0)-P_{RACS}(T>T_0)-P_{GACS}$$

$$-P_{SMLT}(T>T_0)-(1-\delta_2)P_{RACS}(T<T_0)+\delta_2 P_{SACR}(T<T_0)$$

$$+(1-\delta_1)P_{SDEP}(T<T_0)-P_{MLTS}(T>T_0)+\delta_3 P_{IACR}(T<T_0)$$

$$-(1-\delta_4)P_{WACS}(T<T_0), \qquad (A1e)$$

$$S_{q_g}=(1-\delta_3)P_{RACI}(T<T_0)+P_{GACI}(T<T_0)+P_{GACW}(T<T_0)+P_{GACS}$$

$$+(1-\delta_4)P_{SACW}(T<T_0)+(1-\delta_3)P_{IACR}(T<T_0)+P_{GACR}(T<T_0)$$

$$+P_{GFR}(T<T_0)+(1-\delta_2)P_{RACS}(T<T_0)+(1-\delta_4)P_{WACS}(T<T_0)$$

$$-P_{GMLT}(T>T_0)+(1-\delta_1)P_{GDEP}(T<T_0)-P_{MLTG}(T>T_0)$$

$$+(1-\delta_2)P_{SACR}(T<T_0), \qquad (A1f)$$

where

$$\delta_1=\begin{cases}1 & \text{if } q_c+q_i>10^{-8}gg^{-1}, T<T_0,\\ 0 & \text{otherwise,}\end{cases} \qquad (A2a)$$

$$\delta_2=\begin{cases}1 & \text{if } q_s+q_r<10^{-4}gg^{-1}, T<T_0,\\ 0 & \text{otherwise,}\end{cases} \qquad (A2b)$$

$$\delta_3=\begin{cases}1 & \text{if } q_r>10^{-4}gg^{-1}, T<T_0,\\ 0 & \text{otherwise,}\end{cases} \qquad (A2c)$$

$$\delta_4=\begin{cases}1 & \text{if } q_s\le 10^{-4}gg^{-1}, q_c>5\times 10^{-4}gg^{-1}, T<T_0,\\ 0 & \text{otherwise,}\end{cases} \qquad (A2d)$$

$T_0=0^oC$, and $T_{00}=-35^oC$. The microphysical processes in the terms of the right-hand side of (A1) and corresponding schemes are described in Table A1.

The mathematical formula of cloud microphysical procesess are shown as follow:

$$P_{MLTG} = \frac{2\pi N_{0G}(S-1)}{\rho(A'+B')}[\frac{0.78}{\lambda_G^2} + 0.31(\frac{\overline{a}\rho}{\mu})^{\frac{1}{2}}(\frac{\rho_0}{\rho})^{\frac{1}{4}}\frac{\Gamma(\overline{b}/2+5/2)}{\lambda_G^{\overline{b}/2+5/2}}], \qquad (A3)$$

where $N_{0G}(= 4\times10^6\ m^{-4})$ is the intercept value in graupel size distribution; S is the saturation ratio with respect to water; $\overline{a}(= 19.3\ m^{1-\overline{b}}s^{-1})$ is the constant in fallspeed relation for graupel; $\overline{b}(= 0.37)$ is the fallspeed exponent for graupel; $A' = \frac{L_v}{K_aT}(\frac{L_vM_w}{RT} - 1)$; $B' = \frac{RT}{\chi M_w e_{ws}}$ (Pruppacher and Klett 1978); $K_a(= 2.43\times10^{-2}\ Jm^{-1}s^{-1}K^{-1})$ is the thermal conductivity coefficient of air; $M_w = 18.0160$ is the molecular weight of water; $\chi(= 2.26\times10^{-5}\ m^2s^{-1})$ is the diffusivity coefficient of water vapor in air; $R(= 8.314\times10^3 Jkmol^{-1}K^{-1})$ is the universal gas constant; $e_{ws}(= Nm^{-2})$ is the saturation vapor pressure for water; $\lambda_G[= (\frac{\pi\rho_G N_{0G}}{\rho q_g})^{\frac{1}{4}}]$ is the slope of graupel size distribution; $\rho_G(= 400kgm^{-3})$ is the density of graupel; $\mu(= 1.718\times10^{-5}\ kgm^{-1}s^{-1})$ is the dynamic viscosity of air; Γ is the Gamma function.

$$P_{MLTS} = \frac{4N_{0S}(S-1)}{\rho(A'+B')}[\frac{0.65}{\lambda_S^2} + 0.44(\frac{a''\rho}{\mu})^2(\frac{\rho_0}{\rho})^{\frac{1}{4}}\frac{\Gamma(b/2+5/2)}{\lambda_S^{b/2+5/2}}], \qquad (A4)$$

where $N_{0S}(= 4\times10^6\ m^{-4})$ is the intercept value in snowflake size distribution; $a''(= 1.139\ m^{1-b}s^{-1})$ is the constant in fallspeed relation for snow; $b(= 0.11)$ is the fallspeed exponent for snow; $\lambda_S[= (\frac{\pi\rho_S N_{0S}}{\rho q_s})^{\frac{1}{4}}]$ is the slope of snow size distribution; $\rho_S(= 100kgm^{-3})$ is the density of snow.

$$P_{REVP} = \frac{2\pi N_{0R}(S-1)}{\rho(A'+B')}[\frac{0.78}{\lambda_R^2} + 0.31(\frac{a'\rho}{\mu})^{\frac{1}{2}}(\frac{\rho_0}{\rho})^{\frac{1}{4}}\frac{\Gamma(3)}{\lambda_R^3}], \qquad (A5)$$

where $N_{0R}(= 8\times10^6\ m^{-4})$ is the intercept value in raindrop size distribution; $a'(= 3\times10^3\ s^{-1})$ is the constant in linear fallspeed relation for rain; $\lambda_R[= (\frac{\pi\rho_L N_{0R}}{\rho q_r})^{\frac{1}{4}}]$ is the slope of snow size distribution; $\rho_L(= 10^3kgm^{-3})$ is the density of snow.

$$P_{IMLT} = \frac{q_i}{\Delta t}, \qquad (A6)$$

where Δt is the time step.

$$P_{CND} = \frac{1}{\Delta t}\frac{T - T_{00}}{T_0 - T_{00}}\frac{q_v - (q_{ws} + q_{is})}{1 + (\frac{A_1 q_c q_{ws}}{q_c + q_i} + \frac{A_2 q_i q_{is}}{q_c + q_i})(\frac{L_v}{c_p}\frac{T - T_{00}}{T_0 - T_{00}} + \frac{L_s}{c_p}\frac{T_0 - T}{T_0 - T_{00}})}, \qquad (A7)$$

where q_{ws} and q_{is} are the saturation mixing ratio for water and ice respectively; $A_1 = \frac{237.3B_1}{(T-35.86)^2}$; $A_2 = \frac{265.5B_2}{(T-7.66)^2}$; $B_1 = 17.2693882$; $B_2 = 21.8745584$.

$$P_{GMLT} = \frac{-2\pi}{\rho L_f}K_a(T - T_0)N_{0G}[\frac{0.78}{\lambda_G^2} + 0.31(\frac{\overline{a}\rho}{\mu})^{\frac{1}{2}}(\frac{\rho_0}{\rho})^{\frac{1}{4}}\frac{\Gamma(\overline{b}/2 + 5/2)}{\lambda_G^{\overline{b}/2+5/2}}], \qquad (A8)$$

$$P_{SMLT} = \frac{-2\pi}{\rho L_f}K_a(T - T_0)N_{0S}[\frac{0.65}{\lambda_S^2} + 0.44(\frac{a''\rho}{\mu})^{\frac{1}{2}}(\frac{\rho_0}{\rho})^{\frac{1}{4}}\frac{\Gamma(b/2 + 5/2)}{\lambda_S^{b/2+5/2}}], \qquad (A9)$$

$$P_{RACI} = \frac{\pi}{4}q_i E_{RI} N_{0R}(\frac{\rho_0}{\rho})^{\frac{1}{2}}[\frac{a_0\Gamma(3)}{\lambda_R^3} + \frac{a_1\Gamma(4)}{\lambda_R^4} + \frac{a_2\Gamma(5)}{\lambda_R^5} + \frac{a_3\Gamma(6)}{\lambda_R^6}], \qquad (A10)$$

where $E_{RI}(= 1)$ is the rain/cloud ice collection efficiency; $a_0 = -0.267\ ms^{-1}$, $a_1 = 5.15 \times 10^3\ s^{-1}$, $a_2 = -1.0225 \times 10^6\ m^{-1}s^{-1}$, $a_3 = 7.55 \times 10^7\ m^{-2}s^{-1}$, which are the coefficients in polynomial fallspeed relation for rain.

$$P_{RACW} = \frac{\pi}{4}q_c E_{RC} N_{0R}(\frac{\rho_0}{\rho})^{\frac{1}{2}}[\frac{a_0\Gamma(3)}{\lambda_R^3} + \frac{a_1\Gamma(4)}{\lambda_R^4} + \frac{a_2\Gamma(5)}{\lambda_R^5} + \frac{a_3\Gamma(6)}{\lambda_R^6}], \qquad (A11)$$

where $E_{RC}(= 1)$ is the rain/cloud water collection efficiency.

$$P_{RACS} = E_{SR}\pi^2\frac{\rho_s}{\rho}|\overline{V}_R - \overline{V}_S|N_{0R}N_{0S}(\frac{\rho_0}{\rho})^{\frac{1}{2}}[\frac{5}{\lambda_S^6\lambda_R} + \frac{2}{\lambda_S^5\lambda_R^2} + \frac{0.5}{\lambda_S^4\lambda_R^3}], \qquad (A12)$$

where $E_{SR}(= 1)$ is the snow/rain collection efficiency; $\overline{V}_R[= (-0.267 + \frac{206}{\lambda_R} - \frac{2.045\times10^3}{\lambda_R^2} + \frac{9.06\times10^3}{\lambda_R^3})(\frac{\rho_0}{\rho})^{\frac{1}{2}}]$ is the mass-weighted fall-speed for rain; $\overline{V}_S[= a''\frac{\Gamma(4+b)}{6\lambda_S^b}(\frac{\rho_0}{\rho})^{\frac{1}{2}}]$ is the mass-weighted fall-speed for snow.

$$P_{RAUT} = \alpha(q_c - q_0), \qquad (A13)$$

where $\alpha(=10^{-3}s^{-1})$ is the rate coefficient for autoconversion; $q_0(=1.25\times10^{-3}gg^{-1})$ is the mixing ratio threshold.

$$P_{IDW}=\frac{n_0e^{0.5|T-T_0|}}{1000\rho}b_1(\frac{q_i\rho}{n_0e^{0.5|T-T_0|}})^{b_2}, \tag{A14}$$

where $n_0=10^{-8}m^{-3}$; b_1 and b_2 are the positive temperature-dependent coefficients tabulated by Koenig (1971).

$$P_{IACR}=n_{ci}E_{RI}\frac{\pi^2}{24}\frac{\rho_L}{\rho}N_{0R}(\frac{\rho_0}{\rho})^{\frac{1}{2}}[\frac{a_0\Gamma(6)}{\lambda_R^6}+\frac{a_1\Gamma(7)}{\lambda_R^7}+\frac{a_2\Gamma(8)}{\lambda_R^8}+\frac{a_3\Gamma(9)}{\lambda_R^9}], \tag{A15}$$

where $n_{ci}(=\frac{\rho q_i}{\overline{M}_i})$ is the number concentration of cloud ice crystals; $\overline{M}_i(=6\times10^{-12}kg)$ is the average mass of a cloud ice particle.

$$P_{IHOM}=\frac{q_c}{\Delta t}, \tag{A16}$$

$$P_{DEP}=\frac{1}{\Delta t}\frac{T_0-T}{T_0-T_{00}}\frac{q_v-(q_{ws}+q_{is})}{1+(\frac{A_1q_cq_{ws}}{q_c+q_i}+\frac{A_2q_iq_{is}}{q_c+q_i})(\frac{L_v}{c_p}\frac{T-T_{00}}{T_0-T_{00}}+\frac{L_s}{c_p}\frac{T_0-T}{T_0-T_{00}})}, \tag{A17}$$

$$P_{SAUT}=\frac{\rho q_i-M_{max}n_0e^{-0.6(T-T_0)}}{\rho\Delta t}, \tag{A18}$$

where $M_{max}(=9.4\times10^{-10}kg)$ is the maximum allowed crystal mass.

$$P_{SACI}=\frac{\pi a''q_iE_{SI}N_{0S}}{4}(\frac{\rho_0}{\rho})^{\frac{1}{2}}\frac{\Gamma(b+3)}{\lambda_S^{b+3}}, \tag{A19}$$

where $E_{SI}(=0.1)$ is the snow/cloud ice collection efficiency.

$$P_{SACW}=\frac{\pi a''q_cE_{SC}N_{0S}}{4}(\frac{\rho_0}{\rho})^{\frac{1}{2}}\frac{\Gamma(b+3)}{\lambda_S^{b+3}}, \tag{A20}$$

where $E_{SC}(=1)$ is the snow/cloud water collection efficiency.

$$P_{SFW} = \frac{q_i \Delta t}{m_{ir} \Delta t_1}(b_1 m_{ir}^{b_2} + \pi \rho q_c r^2 U_{ir}), \tag{A21}$$

where $\Delta t_1 [= \frac{1}{b_1(1-b_2)}(m_{ir}^{1-b_2} - m_{ir_0}^{1-b_2})]$ is the timescale needed for a crystal to grow from radius r_0 to radius r; $m_{ir}(= 3.84 \times 10^{-9} kg)$ and $U_{ir}(= 1 ms^{-1})$ are the mass and terminal velocity of an ice crystal $r(= 100 \mu m)$; $m_{ir}(= 2.46 \times 10^{-10} kg)$ is the mass of an ice crystal $r_0(= 40 \mu m)$.

$$P_{SFI} = \frac{q_i}{\Delta t_1}, \tag{A22}$$

$$P_{SACR} = E_{SR} \pi^2 \frac{\rho_L}{\rho} |\overline{V}_S - \overline{V}_R| N_{0R} N_{0S} (\frac{\rho_0}{\rho})^{\frac{1}{2}} [\frac{5}{\lambda_R^6 \lambda_S} + \frac{2}{\lambda_R^5 \lambda_S^2} + \frac{0.5}{\lambda_R^4 \lambda_S^3}], \tag{A23}$$

$$P_{SDEP} = \frac{4 N_{0S}(S_i - 1)}{\rho(A'' + B'')} [\frac{0.65}{\lambda_S^2} + 0.44 (\frac{a'' \rho}{\mu})^{\frac{1}{2}} (\frac{\rho_0}{\rho})^{\frac{1}{4}} \frac{\Gamma(b/2 + 5/2)}{\lambda_S^{b/2+5/2}}], \tag{A24}$$

where S_i is the saturation ratio with respect to ice; $A'' = \frac{L_v}{K_a T}(\frac{L_s M_w}{RT} - 1)$; $B'' = \frac{RT}{\chi M_w e_{is}}$; $e_{is}(= Nm^{-2})$ is the saturation vapor pressure for ice.

$$P_{GACI} = \frac{\pi \overline{a} q_i E_{GI} N_{0G}}{4} (\frac{\rho_0}{\rho})^{\frac{1}{2}} \frac{\Gamma(\overline{b} + 3)}{\lambda_G^{\overline{b}+3}}, \tag{A25}$$

where $E_{GI}(= 0.1)$ is the graupel/cloud ice collection efficiency.

$$P_{GACR} = E_{GR} \pi^2 \frac{\rho_L}{\rho} |\overline{V}_G - \overline{V}_R| N_{0R} N_{0G} (\frac{\rho_0}{\rho})^{\frac{1}{2}} [\frac{5}{\lambda_R^6 \lambda_G} + \frac{2}{\lambda_R^5 \lambda_G^2} + \frac{0.5}{\lambda_R^4 \lambda_G^3}], \tag{A26}$$

where $E_{GR}(= 1)$ is the graupel/rain collection efficiency; $\overline{V}_G [= \overline{a} \frac{\Gamma(4+\overline{b})}{6 \lambda_G^{\overline{b}}} (\frac{\rho_0}{\rho})^{\frac{1}{2}}]$ is the mass-weighted fall-speed for graupel.

$$P_{GACS} = E_{GS} \pi^2 \frac{\rho_S}{\rho} |\overline{V}_G - \overline{V}_S| N_{0S} N_{0G} (\frac{\rho_0}{\rho})^{\frac{1}{2}} [\frac{5}{\lambda_S^6 \lambda_G} + \frac{2}{\lambda_S^5 \lambda_G^2} + \frac{0.5}{\lambda_S^4 \lambda_G^3}], \tag{A27}$$

where $E_{GS}(=0.1)$ is the graupel/snow collection efficiency.

$$P_{GACW} = \frac{\pi \bar{a} q_c E_{GC} N_{0G}}{4} (\frac{\rho_0}{\rho})^{\frac{1}{2}} \frac{\Gamma(\bar{b}+3)}{\lambda_G^{\bar{b}+3}}, \tag{A28}$$

where $E_{GC}(=1)$ is the graupel/cloud water collection efficiency.

$$P_{WACS} = \overline{n}_c E_{SC} a'' \frac{\pi^2}{24} \frac{\rho_S}{\rho} N_{0R} (\frac{\rho_0}{\rho})^{\frac{1}{2}} \frac{\Gamma(b+6)}{\lambda_S^{b+6}}, \tag{A29}$$

where $\overline{n}_c(=\frac{\rho q_c}{\overline{M}_c})$ is the number concentration of cloud water droplets; $\overline{M}_c(=4\times10^{-12})$ is the average mass of cloud water droplet.

$$P_{GDEP} = \frac{2\pi N_{0G}(\overline{S}_i - 1)}{\rho(A'' + B'')} [\frac{0.78}{\lambda_G^2} + 0.31 (\frac{\bar{a}\rho}{\mu})^{\frac{1}{2}} (\frac{\rho_0}{\rho})^{\frac{1}{4}} \frac{\Gamma(\bar{b}/2+5/2)}{\lambda_G^{\bar{b}/2+5/2}}], \tag{A30}$$

$$P_{GFR} = 20\pi^2 B_3 N_{0R} \frac{\rho_L}{\rho} \frac{e^{A_3(T_0-T)}-1}{\lambda_R^7}, \tag{A31}$$

where $A_3(=0.66K^{-1})$ is the constant in Bigg freezing; $B_3(=100m^{-3}s^{-1})$ is the constant in raindrop freezing equation.

Table A1 List of microphysical processes and their parameterization schemes in Appendix

Notation	Description	Scheme
P_{MLTG}	Growth of vapor by evaporation of liquid water from the surface of graupel	RH84
P_{MLTS}	Growth of vapor by evaporation of melting snow	RH83
P_{REVP}	Growth of vapor by evaporation of raindrop	RH83
P_{IMLT}	Growth of cloud water by melting of cloud ice	RH83
P_{CND}	Growth of cloud water by the condensation of supersaturated vapor	TSM
P_{GMLT}	Growth of raindrop by melting of graupel	RH84
P_{SMLT}	Growth of raindrop by melting of snow	RH83
P_{RACI}	Growth of raindrop by the accretion of cloud ice	RH84
P_{RACW}	Growth of raindrop by the collection of cloud water	RH83
P_{RACS}	Growth of raindrop by the accretion of snow	RH84
P_{RAUT}	Growth of raindrop by the autoconversion of cloud water	LFO
P_{IDW}	Growth of cloud ice by the deposition of cloud water	KFLC
P_{IACR}	Growth of cloud ice by the accretion of rain	RH84
P_{IHOM}	Growth of cloud ice by the homogeneous freezing of cloud water	
P_{DEP}	Growth of cloud ice by the deposition of supersaturated vapor	TSM
P_{SAUT}	Growth of snow by the conversion of cloud ice	RH83
P_{SACI}	Growth of snow by the collection of cloud ice	RH83
P_{SACW}	Growth of snow by the accretion of cloud water	RH83
P_{SFW}	Growth of snow by the deposition of cloud water	KFLC
P_{SFI}	Growth of snow by the riming of cloud ice	KFLC
P_{SACR}	Growth of snow by the accretion of raindrop	LFO
P_{SDEP}	Growth of snow by the deposition of vapor	RH83
P_{GACI}	Growth of graupel by the collection of cloud ice	RH84
P_{GACR}	Growth of graupel by the accretion of raindrop	RH84
P_{GACS}	Growth of graupel by the accretion of snow	RH84
P_{GACW}	Growth of graupel by the accretion of cloud water	RH84
P_{WACS}	Growth of graupel by the riming of snow	RH84
P_{GDEP}	Growth of graupel by the vapor deposition	RH84
P_{GFR}	Growth of graupel by the freezing of raindrop	LFO

References

Arakawa, A., and W. H. Schubert, 1974: Interaction of a cumulus cloud ensemble with the large-scale environment, Part I. *J. Atmos. Sci.*, **31**, 674-701.

Grabowski, W. W., X. Wu, and M. W. Moncrieff, 1996: Cloud-resolving model of tropical cloud systems during Phase III of GATE. Part I: Two-dimensional experiments. *J. Atmos. Sci.*, **53**, 3684-3709.

Koenig, L. R., 1971: Numerical modeling of ice deposition. *J. Atmos. Sci.*, **28**, 226-237.

Krueger, S. K., Q. Fu, K. N. Liou and H.-N. S. Chin, 1995: Improvement of an ice-phase microphysics parameterization for use in numerical simulations of tropical convection. *J. Appl. Meteor.*, **34**. 281-287.

Kuo, H. L., 1965: On formation and intensification of tropical cyclones through latent heat release by cumulus convection. *J. Atmos. Sci.*, **22**, 40-63.

Kuo, H. L., 1974: Further studies of the parameterization of the influence of cumulus convection on large-scale flow. *J. Atmos. Sci.*, **31**, 1232-1240.

Li, X., C.-H. Sui, K.-M. Lau, and M.-D. Chou, 1999: Large-scale forcing and cloud-radiation interaction in the tropical deep convective regime. *J. Atmos. Sci.*, **56**, 3028-3042.

Lin, Y.-L., R. D. Farley, and H. D. Orville, 1983: Bulk parameterization of the snow field in a cloud model. *J. Climate Appl. Meteor.*, **22**, 1065-1092.

Liu, Y., D.-L. Zhang, and M. K. Yau, 1997: A multiscale numerical study of Hurricane Andrew (1992). Part I: Explicit simulation and Verification. *Mon. Wea. Rev.*, **125**, 3073-3093.

Lord, S. J., H. E. Willoughby, and J. M. Piotrowicz, 1984: Role of a parameterized ice-phase microphysics in an axisymmetric, nonhydrostatic tropical cyclone model. *J. Atmos. Sci.*, **41**, 2836-2848.

Pruppacher, H. R., and J. D. Klett, 1978: Microphysics of clouds and precipitation. Reidel, 714pp.

Rutledge, S. A., and P. V. Hobbs, 1983: The mesoscale and microscale structure and organization of clouds and precipitation in midlatitude cyclones. Part VIII: A model for the "seeder-feeder" process in warm-frontal rainbands. *J. Atmos. Sci.*, **40**, 1185-1206.

Rutledge, S. A., and P. V. Hobbs, 1984: The mesoscale and microscale structure and organization of clouds and precipitation in midlatitude cyclones. Part XII: A disgnostic modeling study of precipitation development in narrow cold-frontal rainbands. *J. Atmos. Sci.*, **41**, 2949-2972.

Soong, S. T., and Y. Ogura, 1980: Response of tradewind cumuli to large-scale processes. *J. Atmos. Sci.*, **37**, 2035-2050.

Soong, S. T., and W. K. Tao, 1980: Response of deep tropical cumulus clouds to mesoscale processes. *J. Atmos. Sci.*, **37**, 2016-2034.

Sui, C.-H., K.-M. Lau, Y. Takayabu, and D. Short, 1997: Diurnal variations in tropical oceanic cumulus ensemble during TOGA COARE. *J. Atmos. Sci.*, **54** 639-655.

Sui, C.-H., X. Li, and K.-M. Lau, 1998: Radiative-convective processes in simulated diurnal variations of tropical oceanic convection. *J. Atmos. Sci.*, **55**, 2345-2359.

Takayabu, Y. N., K.-M. Lau, and C.-H. Sui, 1996: Observation of a quasi-2-day wave during TOGA COARE. *Mon. Wea. Rev.*, **124**, 1892-1913.

Tao, W.-K., and J. Simpson, 1993: The Goddard Cumulus Ensemble model. Part I: Model description. *Terr. Atmos. Oceanic Sci.*, **4**, 35-72.

Tao, W.-K., J. Simpson, and M. McCumber, 1989: An ice-water saturation adjustment. *Mon. Wea. Rev.*, **117**, 231-235.

Weller, R. A., and S. P. Anderson, 1996: Surface meteorology and air-sea fluxes in the western equatorial Pacific warm pool during TOGA COARE. *J. Climate*, **9**, 1959-1990.

Willoughby, H. E., H. L. Jin, S. J. Lord, and J. M. Piotrowicz, 1984: Hurricane structure and evolution as simulated by an axisymmetric, non-hydrostatic numerical model. *J. Atmos. Sci.*, **41**, 1169-1186.

Wu, X., W. W. Grabowski, and M. W. Moncrieff, 1998: Long-term evolution of cloud systems in TOGA COARE and their interactions with radiative and surface processes. Part I: Two-dimensional cloud-resolving model. *J. Atmos. Sci.*, **55**, 2693-2714.

Xu, K.-M., and D. A. Randall, 1996: Explicit simulation of cumulus ensembles with the GATE Phase III data: Comparison with observations. *J. Atmos. Sci.*, **53**, 3710-3736.

Zhang, M. H., and J. L. Lin, 1997: Constrained variational analysis of sounding data based on column-integrated budgets of mass, heat, moisture, and momentum: Approach and application to ARM measurements. *J. Atmos. Sci.*, **54**, 1503-1524.

Figure Captions

Fig. 1 Time evolution of (a) vertical velocity ($mb\ hour^{-1}$), and (b) zonal wind (ms^{-1}) taken from the TOGA COARE for a 20-day period. Downward motion in (a) and westerly wind in (b) are shaded.

Fig. 2 (a) Linear correlation and (b) RMS of the temperature (solid) and specific humidity (dashed) between observation and simulation. The units of RMS in (b) are ^oC for temperature and gkg^{-1} for specific humidity respectively.

Fig. 3 (a) Components of mass-weighted mean heat budget versus local change of mass-weighted mean temperature ($^oCday^{-1}$) and (b) Components of column-integrated moisture budget versus local change of column-integrated specific humidity (precipitable water) ($mmday^{-1}$). Closed dots denote sum of mass-weighted mean latent heat of condensation and vertical potential temperature advection in (a) and sum of vertically-integrated condensation (precipitation) and vertical moisture advection in (b). Open dots represent imposed large-scale horizontal temperature advection in (a) and moisture advection in (b). Symbols "x" are surface sensible heat flux in (a) and surface evaporation flux in (b). Symbols delta denote radiative processes.

Fig. 4 (a) Mass-weighted mean latent heat of condensation versus vertical potential temperature advection ($^oCday^{-1}$), and (b) vertically-integrated condensation (precipitation) versus vertical moisture advection ($mmday^{-1}$).

Fig. 5 (a) Sum of mass-weighted mean latent heat of condensation and vertical potential temperature advection ($^oCday^{-1}$) versus surface rain rate ($mmday^{-1}$), and (b) sum of vertically-integrated condensation and vertical moisture advection ($mmday^{-1}$) versus rain rate ($mmday^{-1}$).

Fig. 6 As Fig. 3a except for those at (a) 194 mb, (b) 309 mb, (c) 487 mb, (d) 694 mb, and (e) 907 mb, and symbols "x" denote vertical heat flux convergence.

Fig. 7 As Fig. 3b except for those at (a) 194 mb, (b) 309 mb, (c) 487 mb, (d) 694 mb, and (e) 907 mb, and symbols "x" denote vertical moisture flux convergence. Note different plotting scales in (a) and (b).

Fig. 8 (a) Column-integrated cloud content versus rain rate in (a)-(c), and (d) vertical profiles

of time-mean cloud contents.

Fig. 9 (a) Column-integrated cloud microphysical processes related to conversions between vapor and cloud contents versus rain rate, and (b) vertical profiles of time-mean cloud microphysical processes.

Fig. 10 Column-integrated cloud microphysical processes related to conversions between cloud water and other cloud contents versus rain rate.

Fig. 11 Column-integrated cloud microphysical processes related to conversions between raindrop and other cloud contents versus rain rate.

Fig. 12 Column-integrated cloud microphysical processes related to conversions between cloud ice and other cloud contents versus rain rate.

Fig. 13 Column-integrated cloud microphysical processes related to conversions between snow and other cloud contents versus rain rate.

Fig. 14 Column-integrated cloud microphysical processes related to conversions between graupel and other cloud contents versus rain rate.

Fig. 15 Vertical profiles of time-mean cloud microphysical processes of (a) cloud water, (b) raindrop, (c) cloud ice, (d) snow, and (e) graupel.

Fig. 16 Mean cloud microphysics budget. Units for cloud contents and conversions are mm and mm day^{-1} respectively.

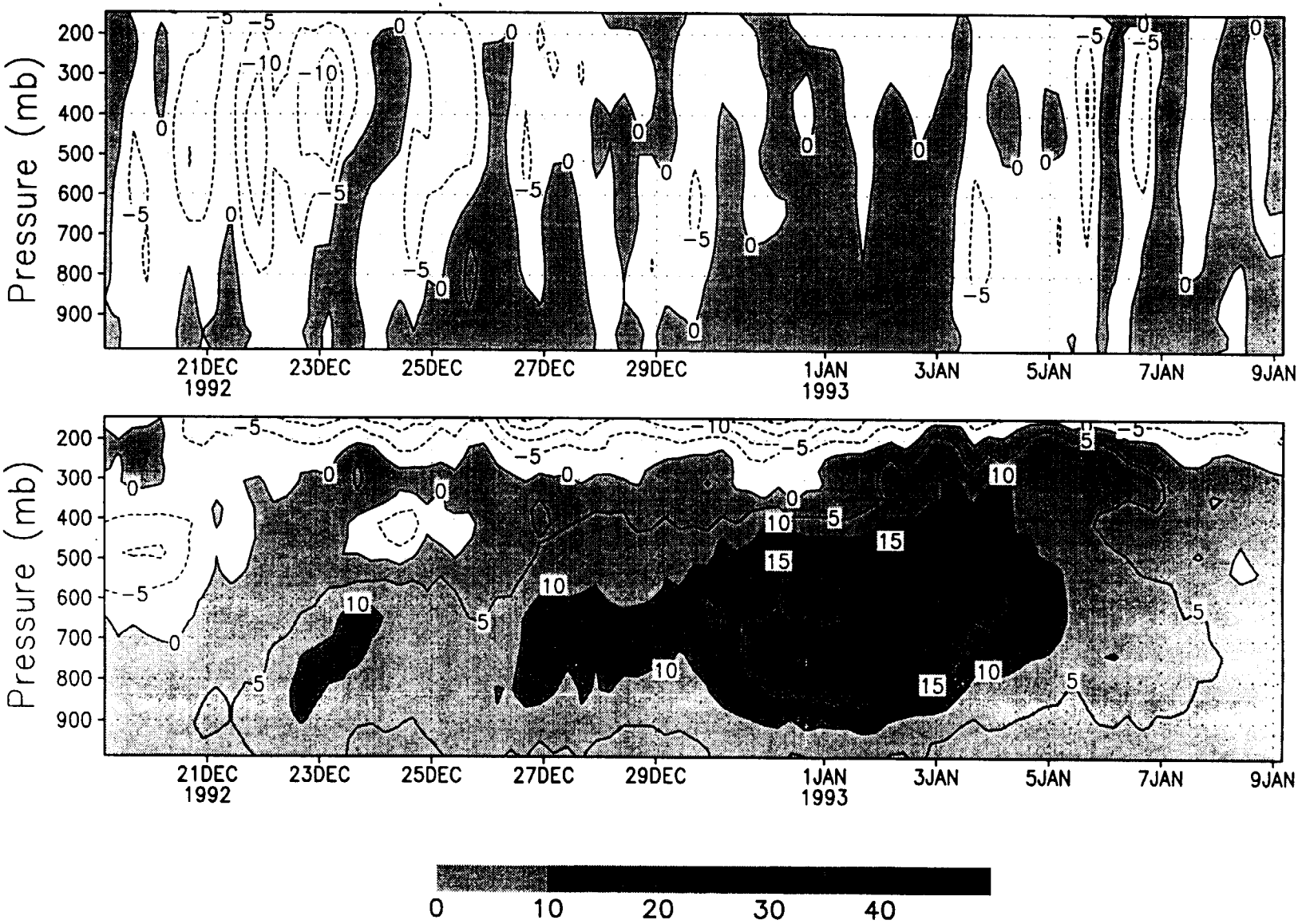
Pressure (mb)
200
300
400
500
600
700
800
900
21DEC
1992
23DEC
25DEC
27DEC
29DEC
1JAN
1993
3JAN
5JAN
7JAN
9JAN
0
10
20
30
40

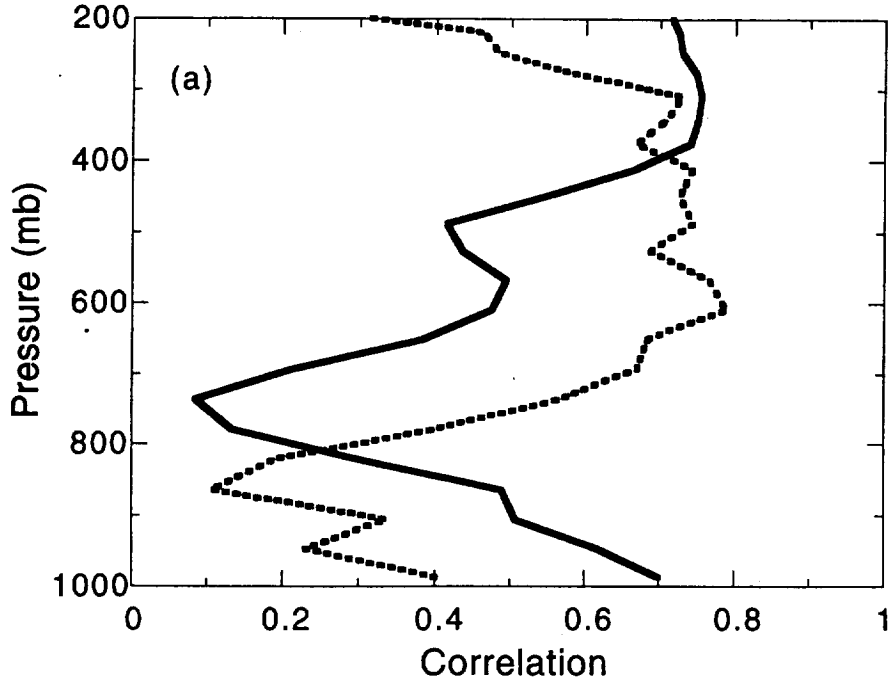
(a)
200
400
600
800
1000
Pressure (mb)
0
0.2
0.4
0.6
0.8
1
Correlation

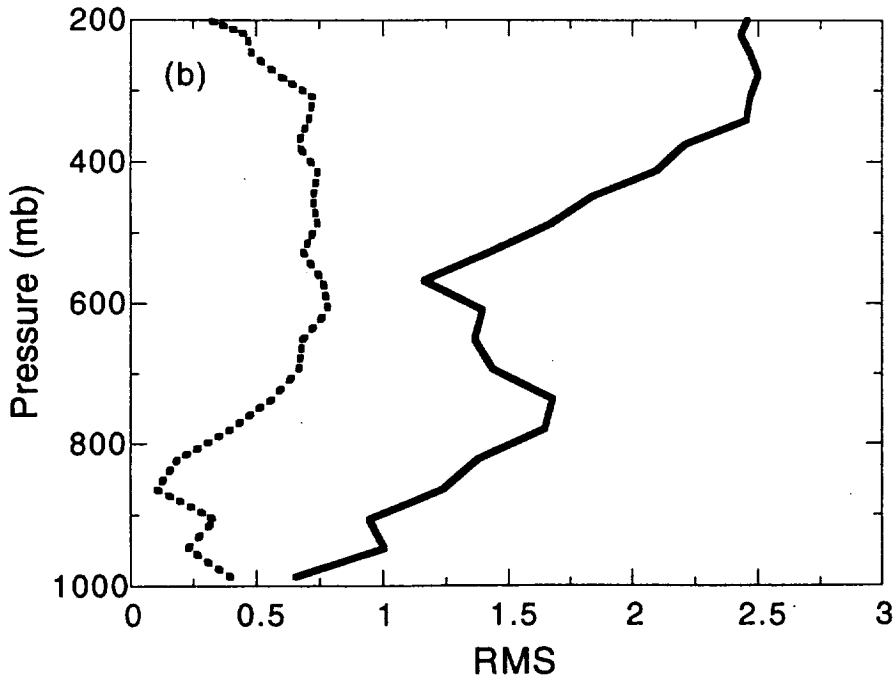
(b)
200
400
600
800
1000
Pressure (mb)
0
0.5
1
1.5
2
2.5
3
RMS

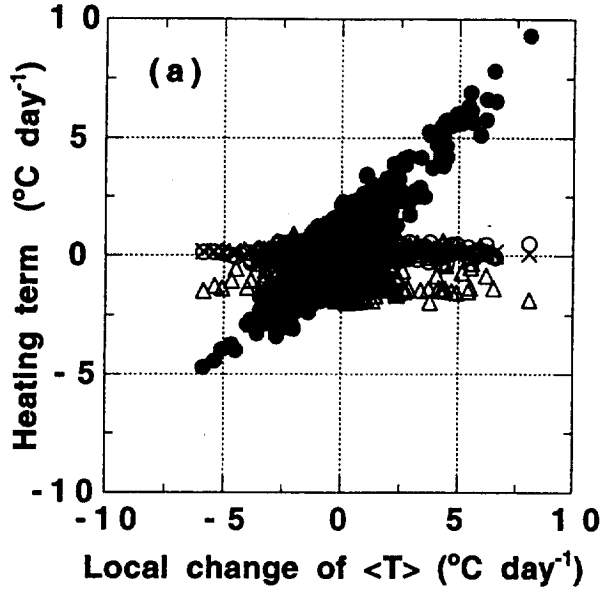
(a)
Heating term (°C day-1)
10
5
0
-5
-10
-10
-5
0
5
10
Local change of <T> (°C day-1)

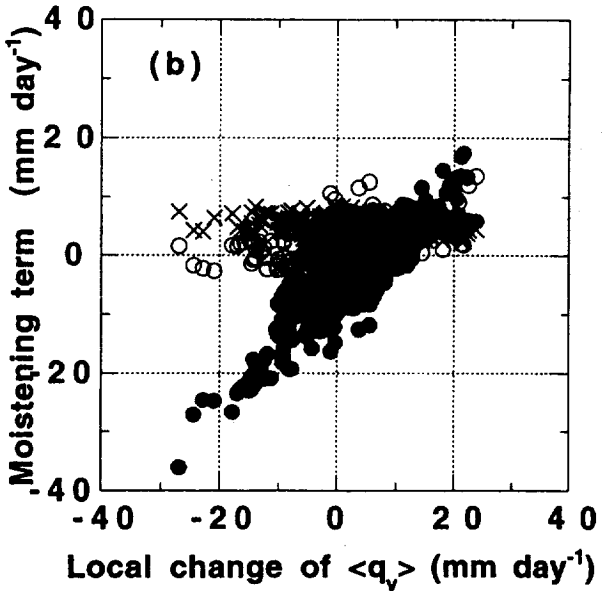
(b)
Moistening term (mm day-1)
40
20
0
-20
-40
-40
-20
0
20
40
Local change of <qv> (mm day-1)

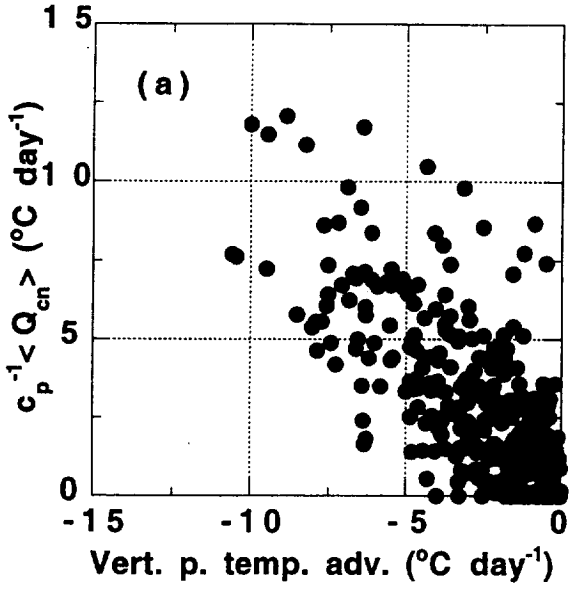
(a)
15
10
5
0
-15
-10
-5
0
$c_p^{-1}< Q_{cn} >$ (°C day^{-1})
Vert. p. temp. adv. (°C day^{-1})

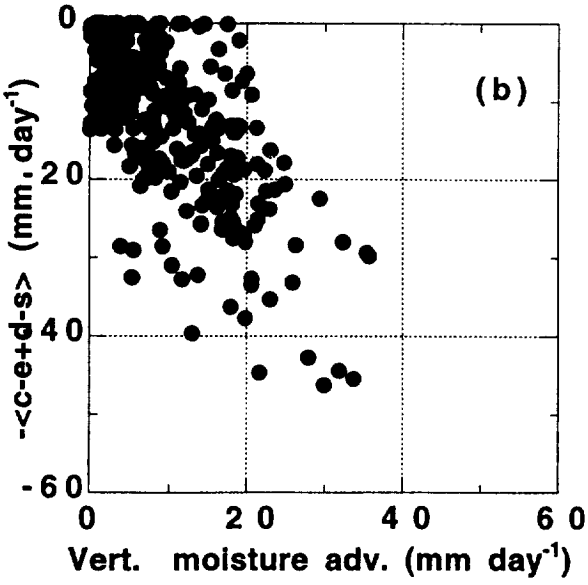
(b)
0
-20
-40
-60
0
20
40
60
-<c-e+d-s> (mm day^{-1})
Vert. moisture adv. (mm day^{-1})

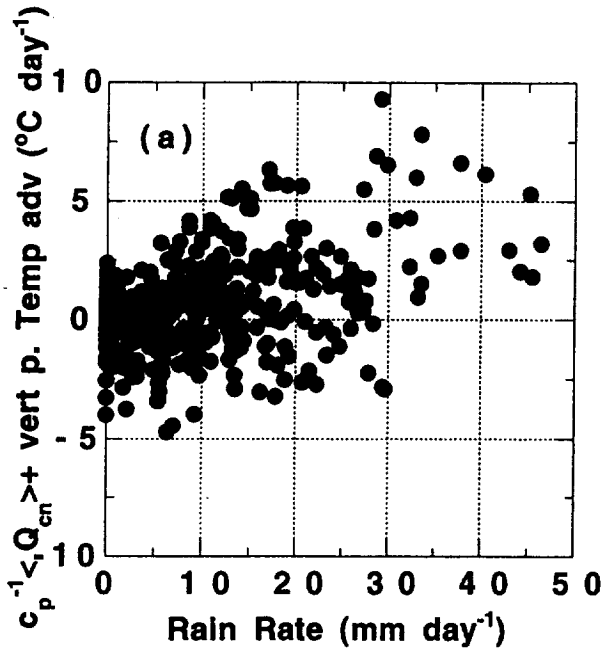
(a)
$c_p^{-1}<\omega, Q_{cn}>$ + vert p. Temp adv (°C day^{-1})
10
5
0
-5
-10
0
10
20
30
40
50
Rain Rate (mm day^{-1})

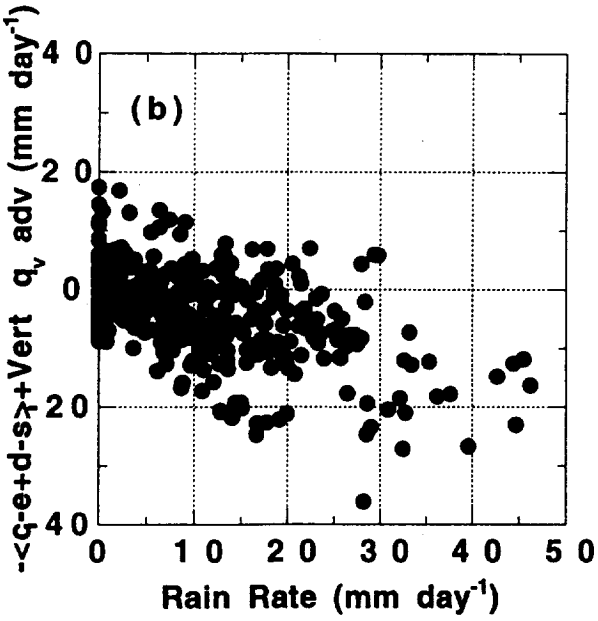
(b)
-<q-e+d-s>+Vert q_v adv (mm day^{-1})
40
20
0
-20
-40
0
10
20
30
40
50
Rain Rate (mm day^{-1})

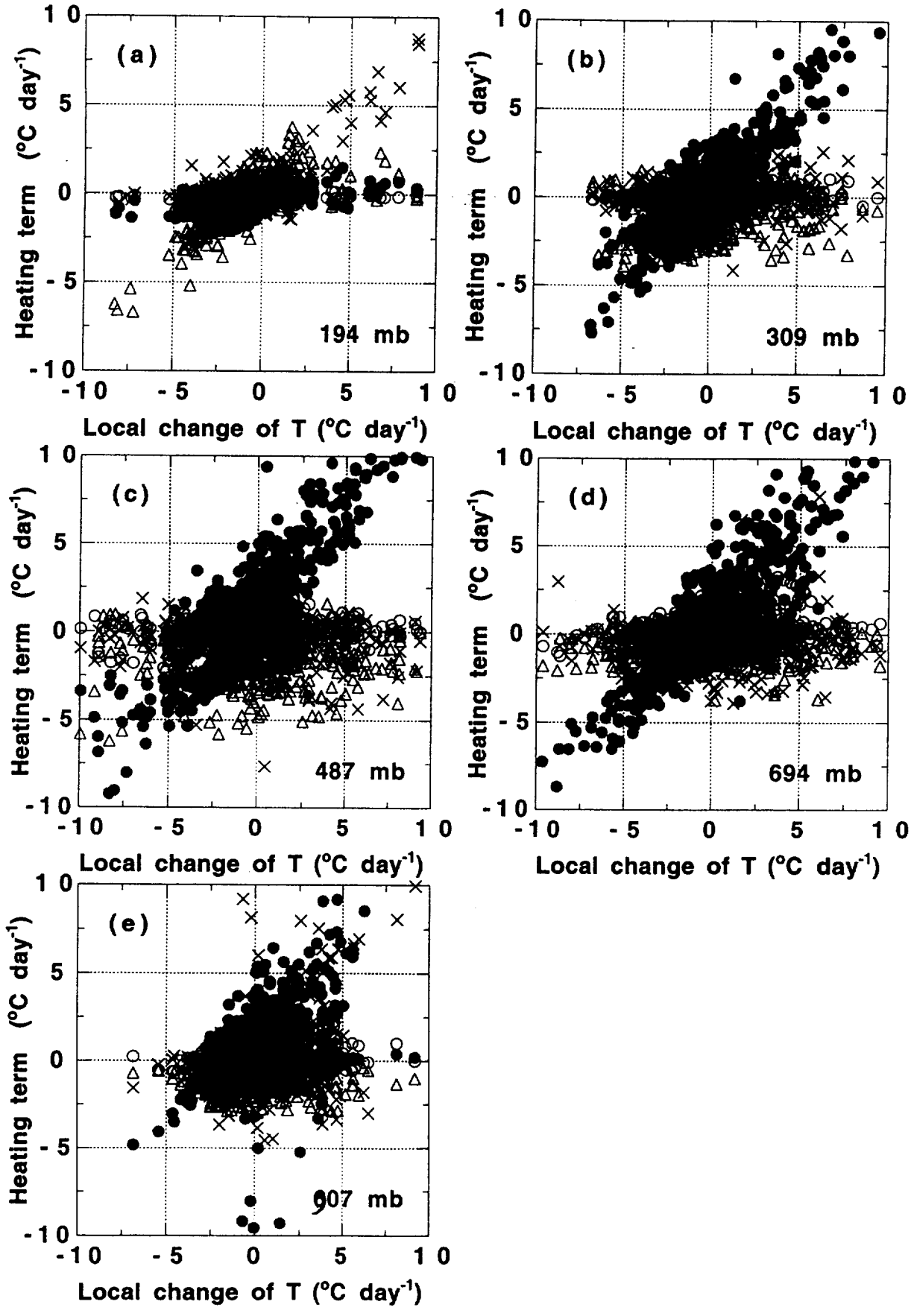
(a)
194 mb
(b)
309 mb
(c)
487 mb
(d)
694 mb
(e)
907 mb
Heating term (°C day-1)
Local change of T (°C day-1)
10
5
0
-5
-10

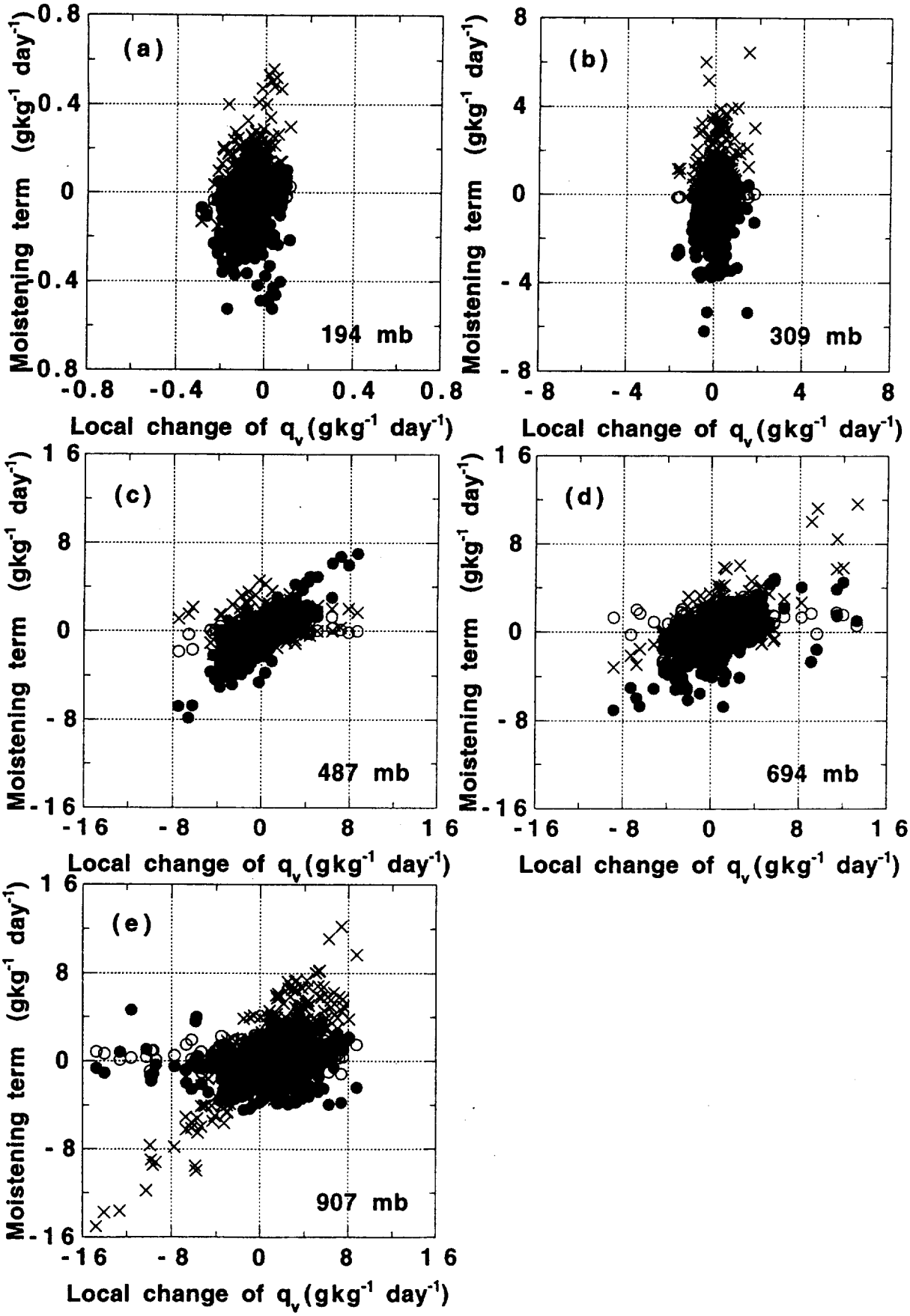
(a)
194 mb
(b)
309 mb
(c)
487 mb
(d)
694 mb
(e)
907 mb
Moistening term (gkg-1 day-1)
Local change of qv (gkg-1 day-1)
0.8
0.4
0
-0.4
-0.8
8
4
-4
-8
16
-16

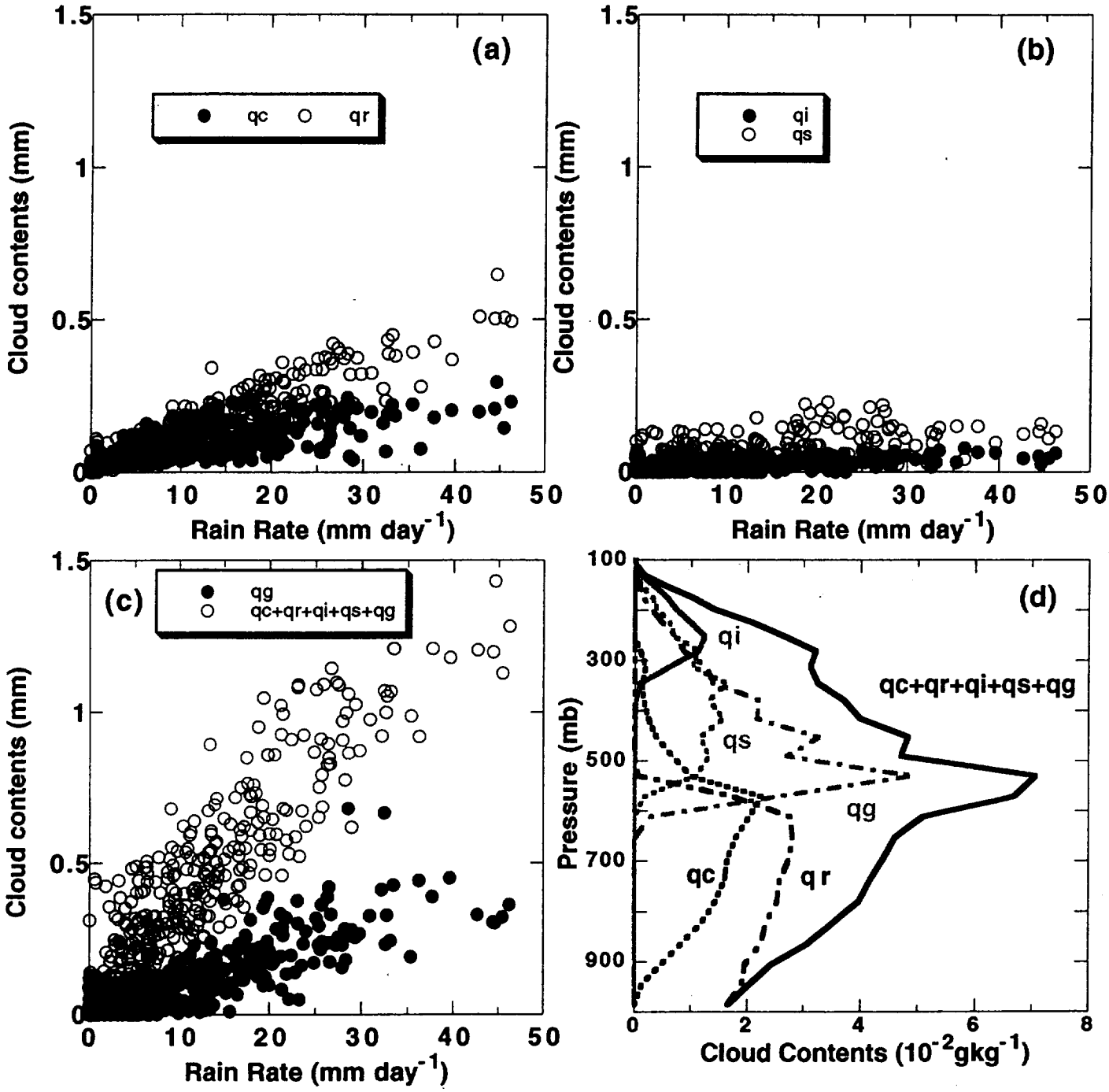
(a)
qc
qr
Cloud contents (mm)
Rain Rate (mm day^{-1})
(b)
qi
qs
Cloud contents (mm)
Rain Rate (mm day^{-1})
(c)
qg
qc+qr+qi+qs+qg
Cloud contents (mm)
Rain Rate (mm day^{-1})
(d)
qi
qc+qr+qi+qs+qg
qs
qg
qc
qr
Pressure (mb)
Cloud Contents (10^{-2}gkg^{-1})

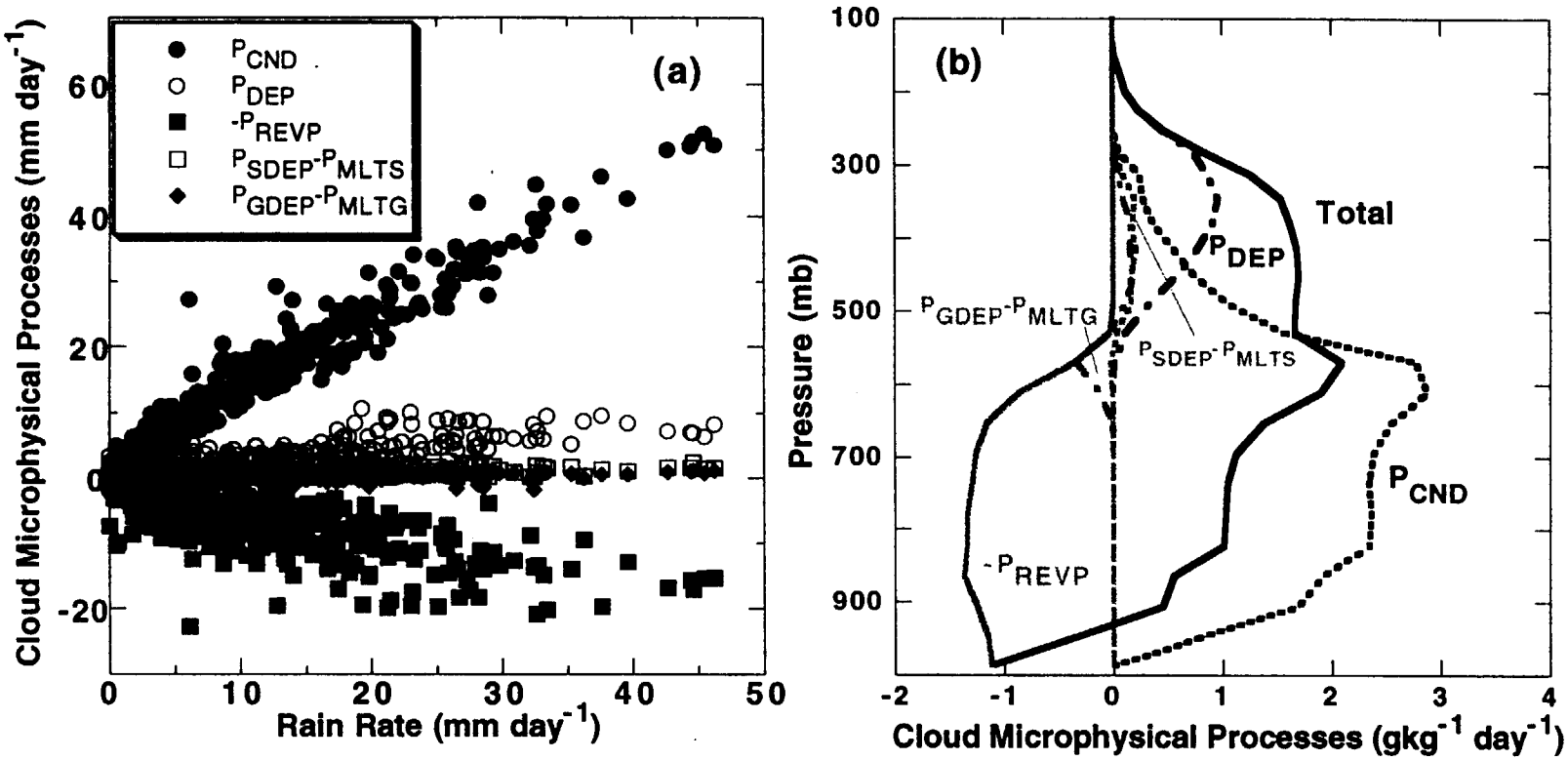
(a)
P_{CND}
P_{DEP}
$-P_{REVP}$
$P_{SDEP}-P_{MLTS}$
$P_{GDEP}-P_{MLTG}$
Cloud Microphysical Processes (mm day^{-1})
Rain Rate (mm day^{-1})
60
40
20
0
-20
0
10
20
30
40
50
(b)
Total
P_{DEP}
$P_{GDEP}-P_{MLTG}$
$P_{SDEP}-P_{MLTS}$
P_{CND}
$-P_{REVP}$
Pressure (mb)
100
300
500
700
900
-2
-1
0
1
2
3
4
Cloud Microphysical Processes (gkg^{-1} day^{-1})

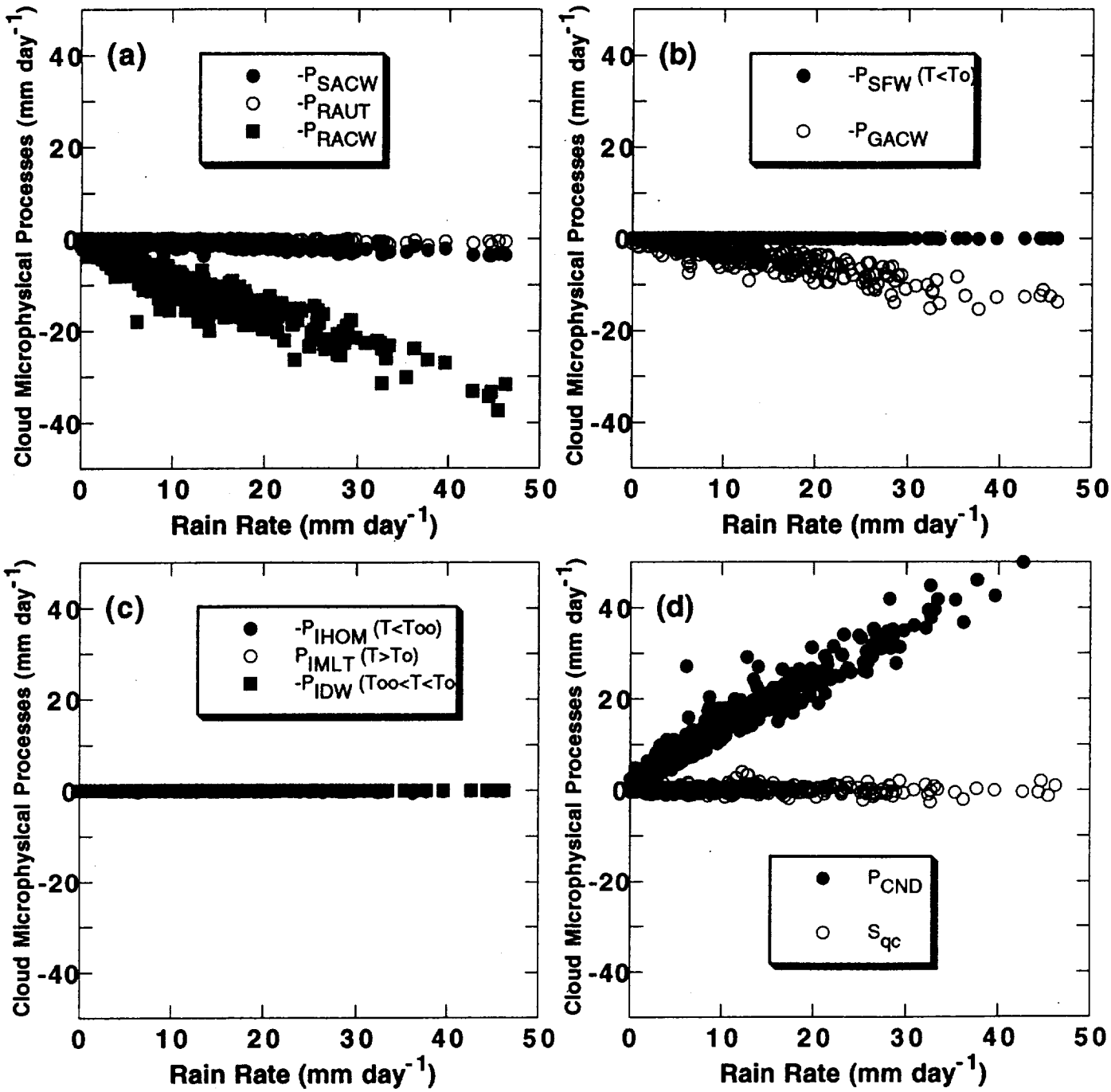
(a)
-P_SACW
-P_RAUT
-P_RACW
(b)
-P_SFW (T<To)
-P_GACW
(c)
-P_IHOM (T<Too)
P_IMLT (T>To)
-P_IDW (Too<T<To)
(d)
P_CND
S_qc
Cloud Microphysical Processes (mm day^-1)
Rain Rate (mm day^-1)
40
20
0
-20
-40
0
10
20
30
40
50

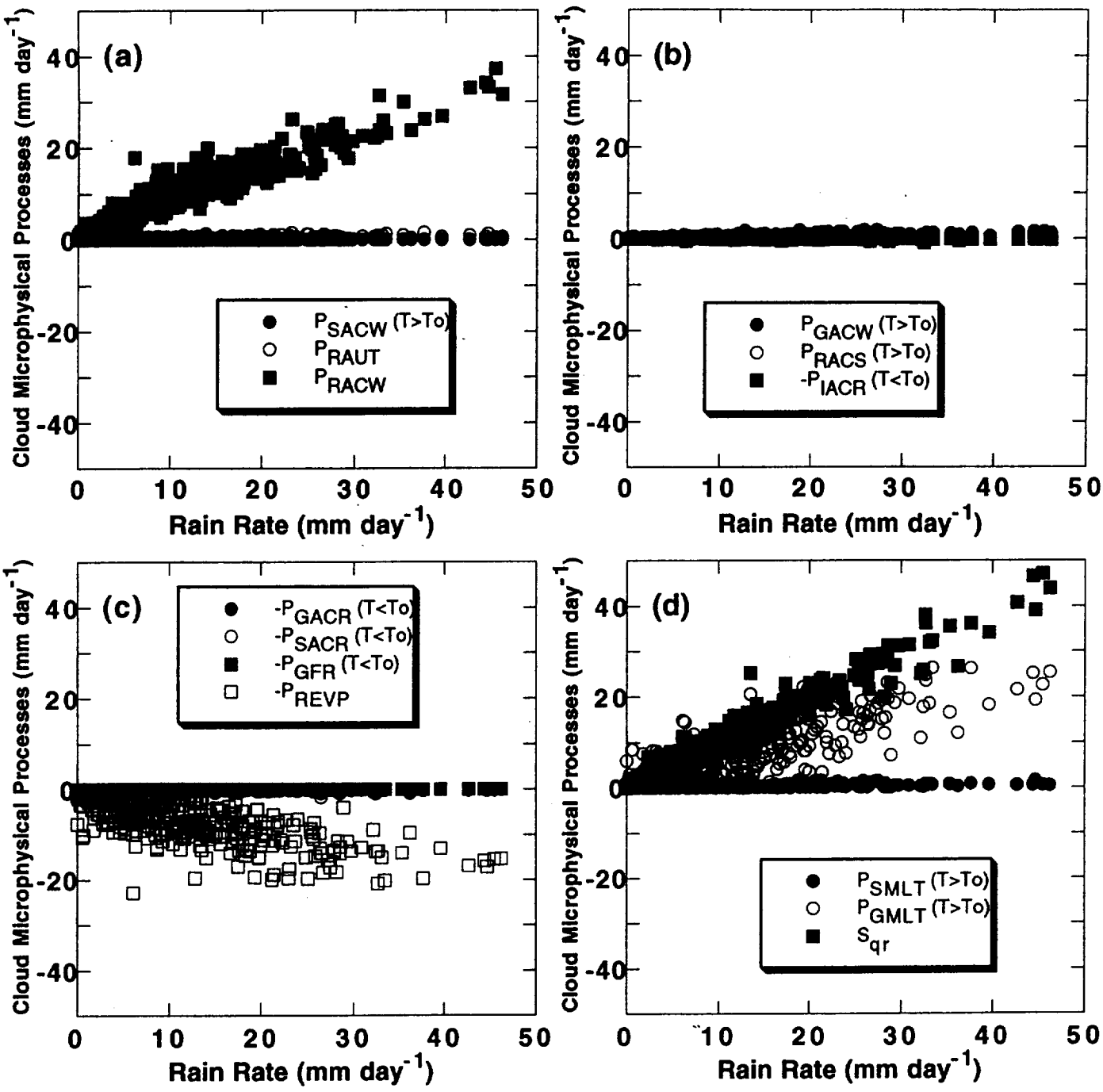
(a)
Cloud Microphysical Processes (mm day-1)
Rain Rate (mm day-1)
PSACW (T>To)
PRAUT
PRACW
(b)
PGACW (T>To)
PRACS (T>To)
-PIACR (T<To)
(c)
-PGACR (T<To)
-PSACR (T<To)
-PGFR (T<To)
-PREVP
(d)
PSMLT (T>To)
PGMLT (T>To)
Sqr

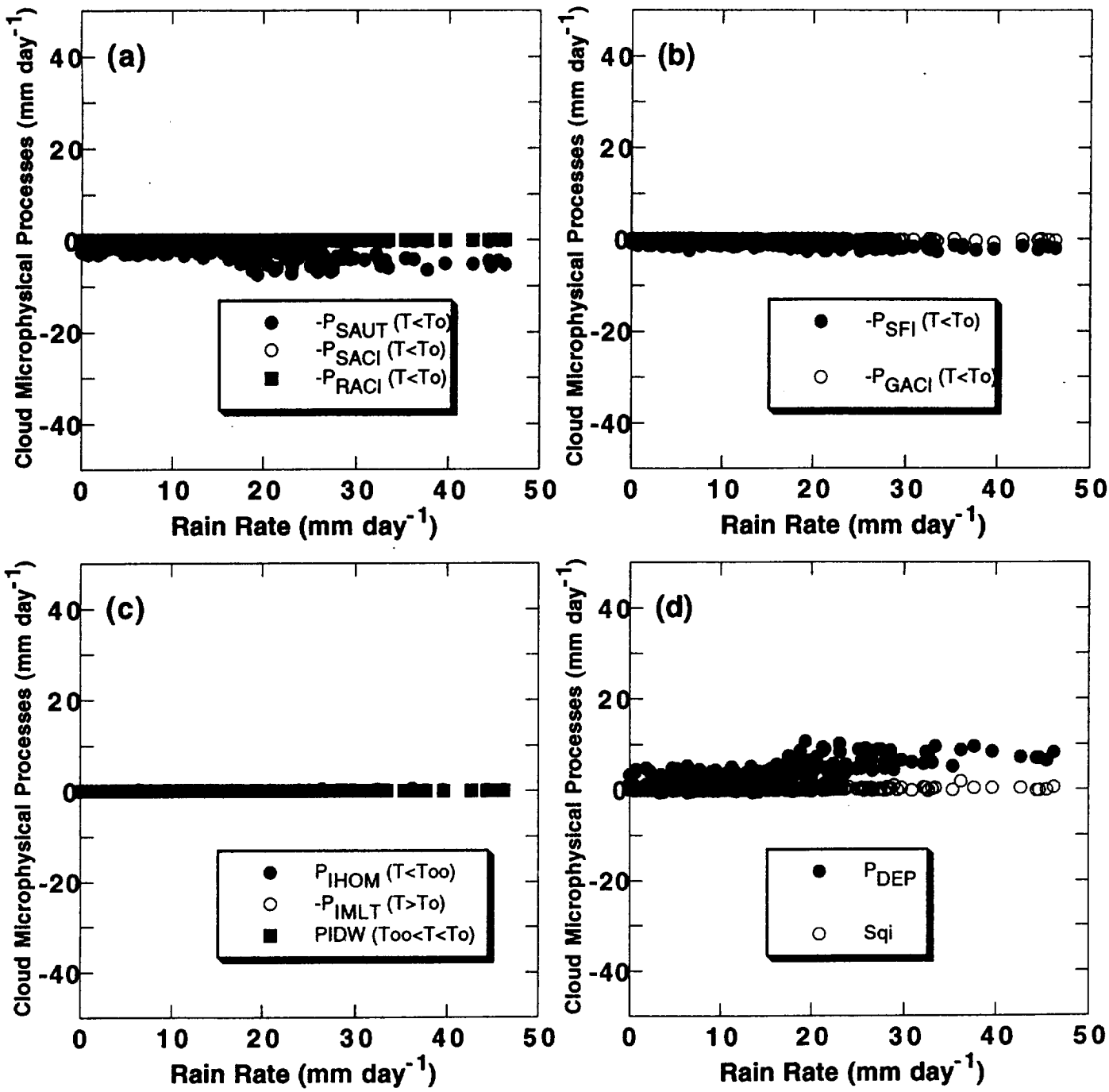
(a)
Cloud Microphysical Processes (mm day-1)
Rain Rate (mm day-1)
-PSAUT (T<To)
-PSACI (T<To)
-PRACI (T<To)
(b)
-PSFI (T<To)
-PGACI (T<To)
(c)
PIHOM (T<Too)
-PIMLT (T>To)
PIDW (Too<T<To)
(d)
PDEP
Sqi

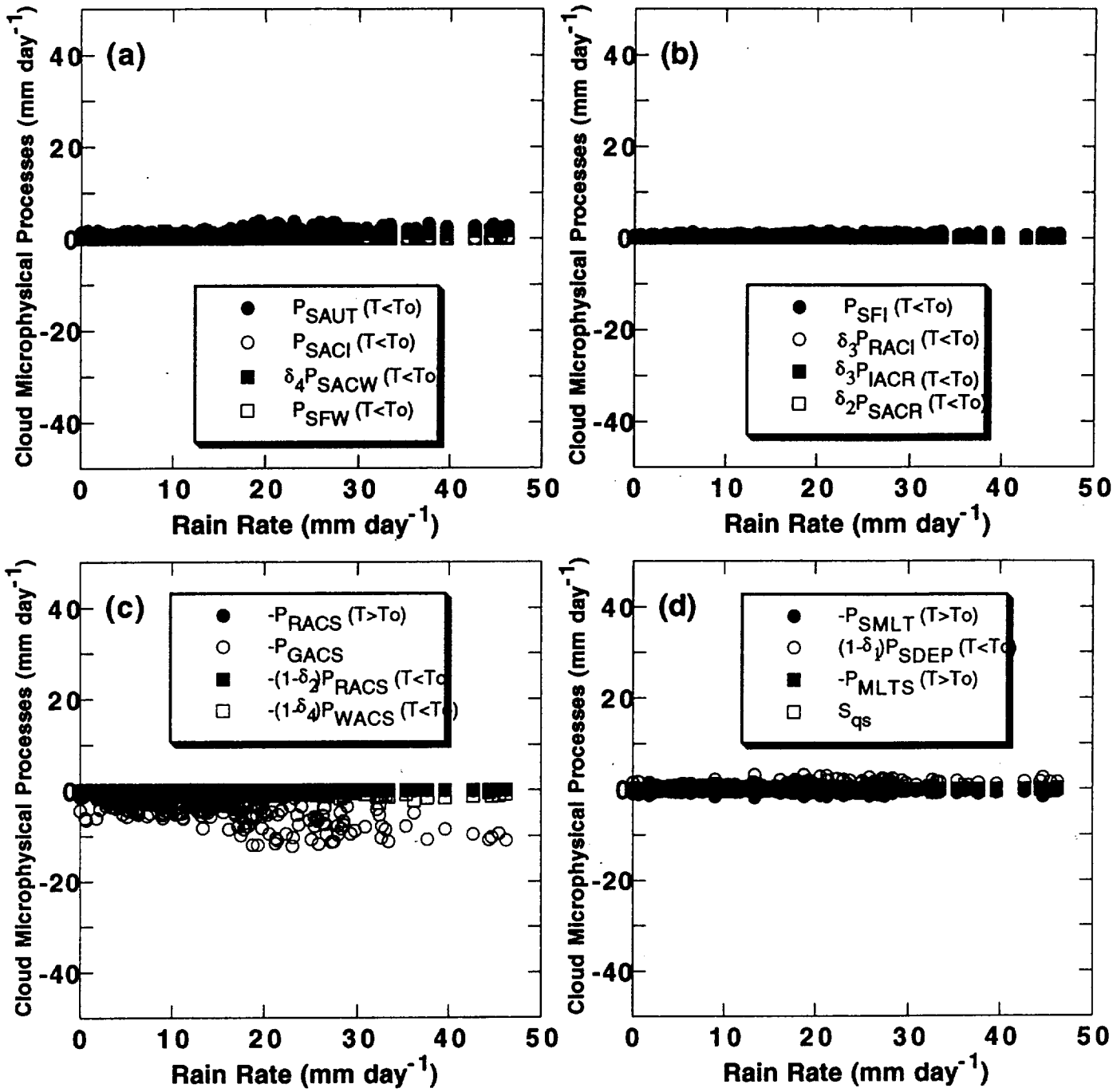
(a)
Cloud Microphysical Processes (mm day^{-1})
Rain Rate (mm day^{-1})
P_{SAUT} (T<To)
P_{SACI} (T<To)
$\delta_4 P_{SACW}$ (T<To)
P_{SFW} (T<To)
(b)
Cloud Microphysical Processes (mm day^{-1})
Rain Rate (mm day^{-1})
P_{SFI} (T<To)
$\delta_3 P_{RACI}$ (T<To)
$\delta_3 P_{IACR}$ (T<To)
$\delta_2 P_{SACR}$ (T<To)
(c)
Cloud Microphysical Processes (mm day^{-1})
Rain Rate (mm day^{-1})
$-P_{RACS}$ (T>To)
$-P_{GACS}$
$-(1-\delta_2)P_{RACS}$ (T<To)
$-(1-\delta_4)P_{WACS}$ (T<To)
(d)
Cloud Microphysical Processes (mm day^{-1})
Rain Rate (mm day^{-1})
$-P_{SMLT}$ (T>To)
$(1-\delta_1)P_{SDEP}$ (T<To)
$-P_{MLTS}$ (T>To)
S_{qs}

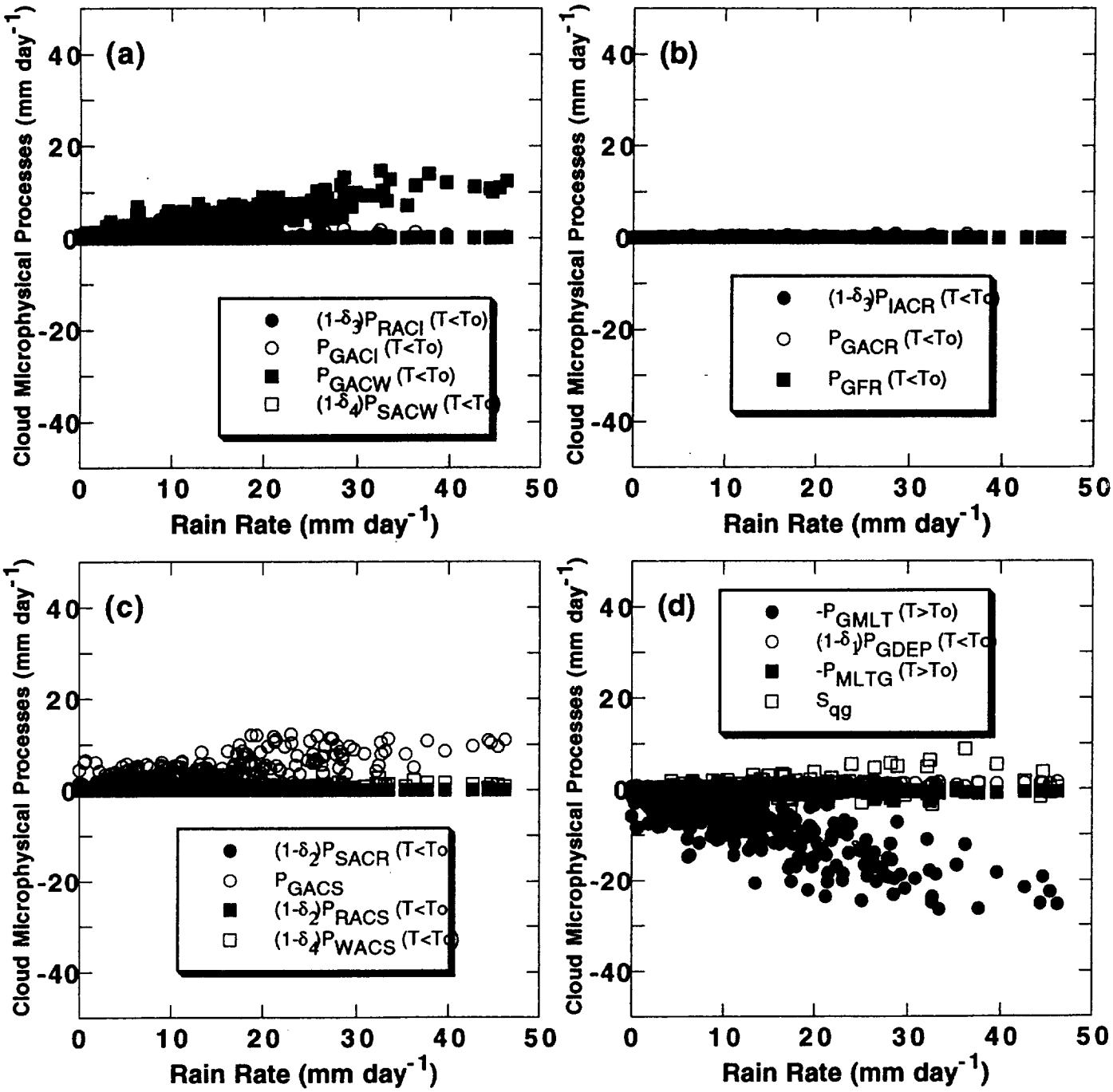
(a)
(b)
(c)
(d)
Cloud Microphysical Processes (mm day^{-1})
Rain Rate (mm day^{-1})
40
20
0
-20
-40
0
10
20
30
40
50
$(1-\delta_3)P_{RACI}$ (T<To)
P_{GACI} (T<To)
P_{GACW} (T<To)
$(1-\delta_4)P_{SACW}$ (T<To)
$(1-\delta_3)P_{IACR}$ (T<To)
P_{GACR} (T<To)
P_{GFR} (T<To)
$(1-\delta_2)P_{SACR}$ (T<To)
P_{GACS}
$(1-\delta_2)P_{RACS}$ (T<To)
$(1-\delta_4)P_{WACS}$ (T<To)
$-P_{GMLT}$ (T>To)
$(1-\delta_1)P_{GDEP}$ (T<To)
$-P_{MLTG}$ (T>To)
S_{qg}

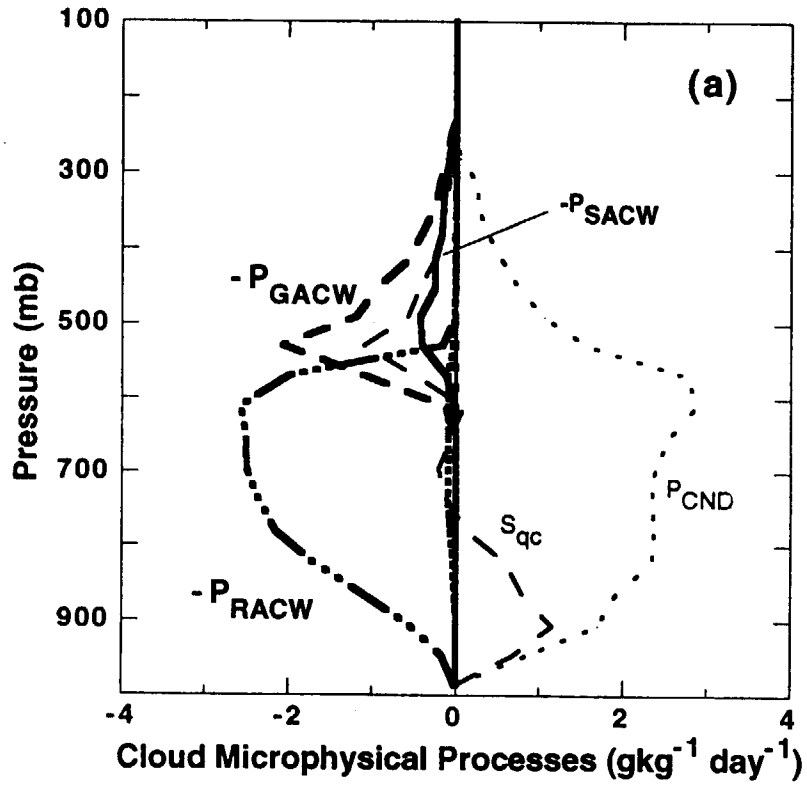
(a)
100
300
500
700
900
Pressure (mb)
-4
-2
0
2
4
Cloud Microphysical Processes (gkg-1 day-1)
-PSACW
-PGACW
PCND
Sqc
-PRACW

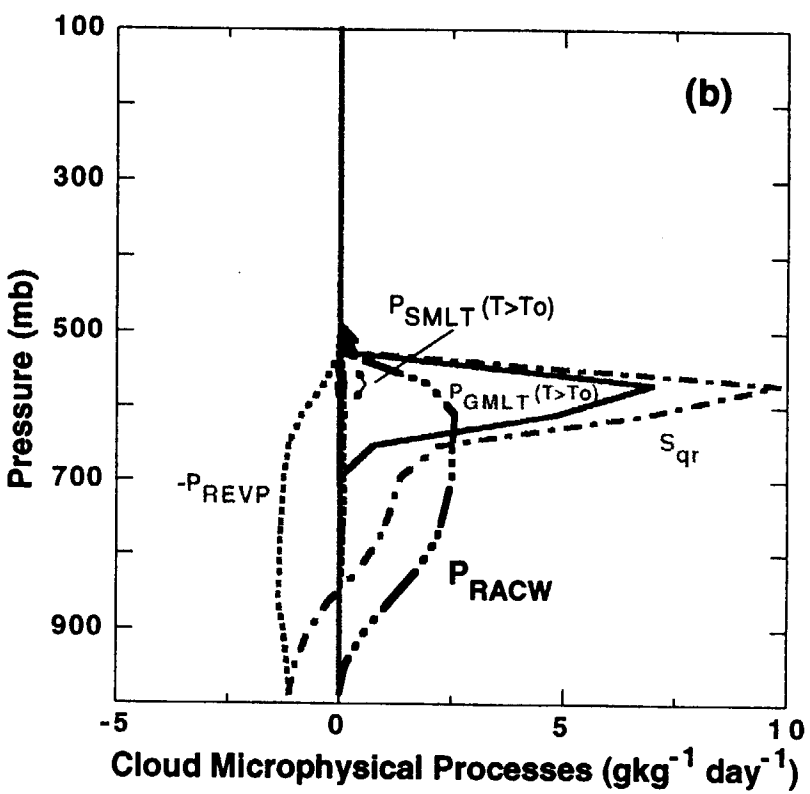
(b)
100
300
500
700
900
Pressure (mb)
-5
0
5
10
Cloud Microphysical Processes (gkg-1 day-1)
PSMLT (T>To)
PGMLT (T>To)
Sqr
-PREVP
PRACW

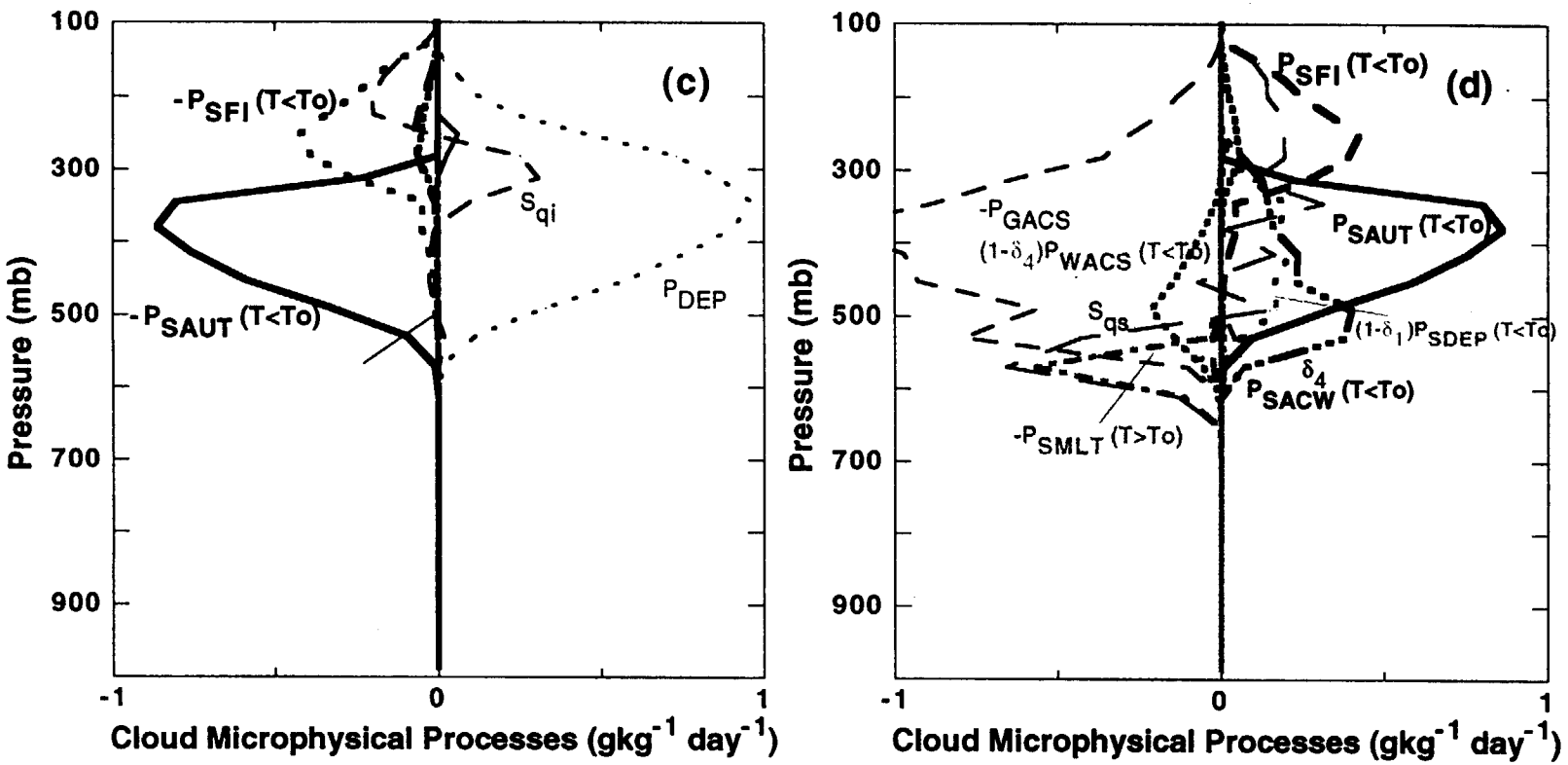
100
300
500
700
900
Pressure (mb)
-1
0
1
Cloud Microphysical Processes (gkg-1 day-1)
(c)
-PSFI (T<To)
Sqi
PDEP
-PSAUT (T<To)
(d)
PSFI (T<To)
-PGACS
(1-δ4)PWACS (T<To)
PSAUT (T<To)
Sqs
(1-δ1)PSDEP (T<To)
δ4
PSACW (T<To)
-PSMLT (T>To)

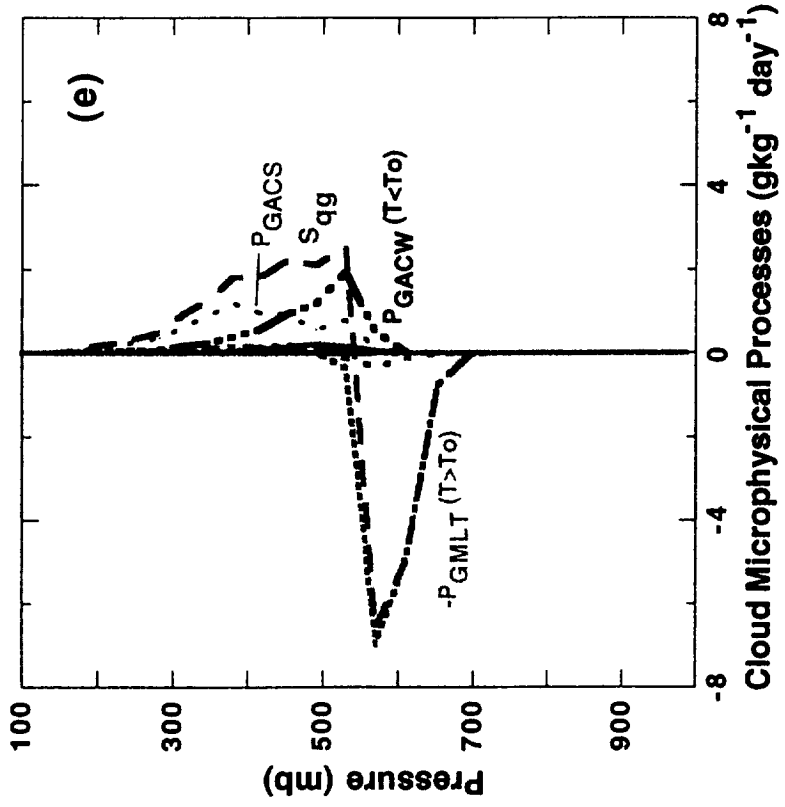
(e)
P_{GACS}
S_{qg}
P_{GACW} (T<To)
$-P_{GMLT}$ (T>To)
Pressure (mb)
100
300
500
700
900
-8
-4
0
4
8
Cloud Microphysical Processes (gkg^{-1} day^{-1})

Mean Cloud Microphysics Budget

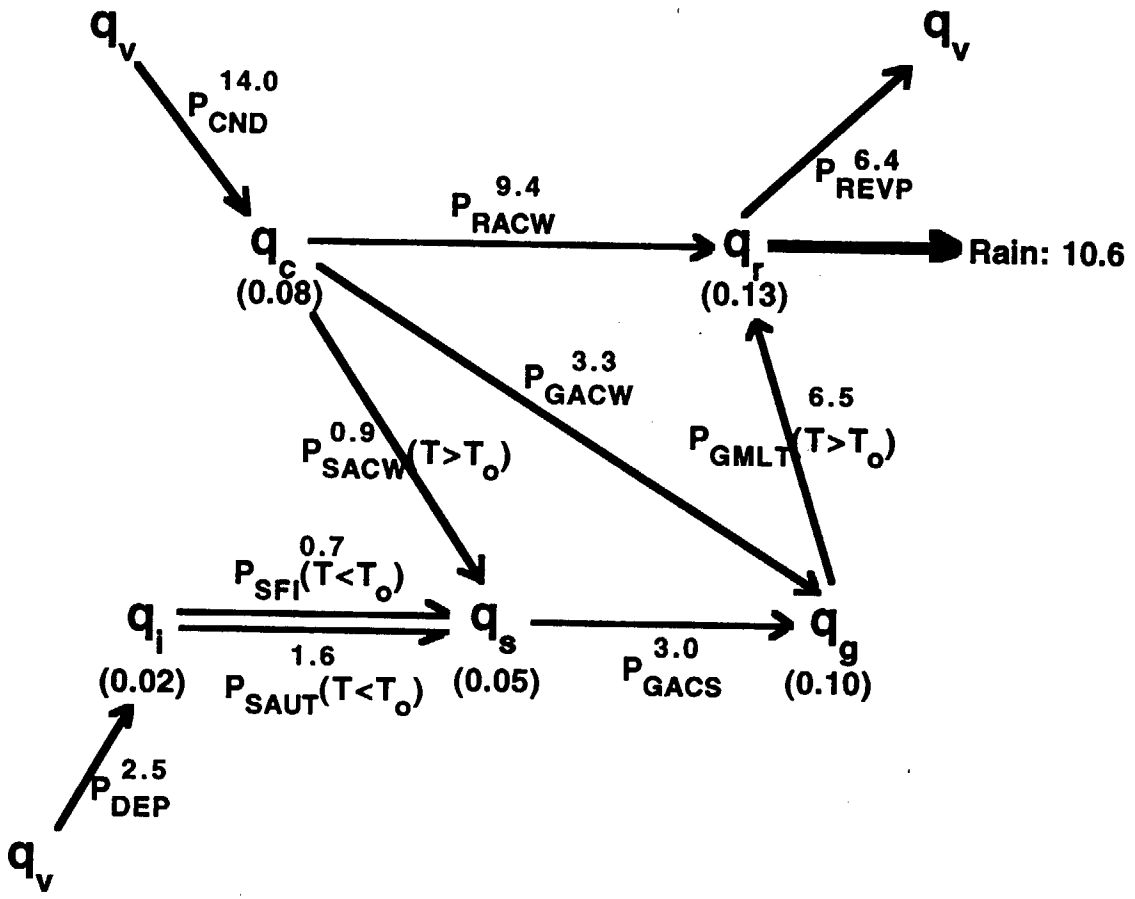

Units: (mm) mm day^{-1}